Three-dimensional biological hydrodynamics study on various types of batoid fishlike locomotion

Namshad Thekkethil ⬤, Atul Sharma ⬤,* and Amit Agrawal ⬤

Department of Mechanical Engineering, Indian Institute of Technology Bombay, Mumbai 400076, India

The present study is on periodic three-dimensional biological flow during batlike flapping as well as fishlike undulation based spanwise symmetric three-dimensional (3D) kinematics and propulsion of batoid fish. For a single parameter based unified study on various types of real and hypothetical batoid fish, a 3D unified-kinematics model is proposed here. Using our immersed interface method based in-house code, the present numerical study is on the effect of various wavelengths (of the wavy undulation of a hydrofoil-shaped lateral cross section) and aspect ratios (of the elliptical span of the body)—corresponding to various types of batoid fishlike locomotion—at a constant nondimensional frequency of 0.5. Furthermore, for *Dasyatis* and a hypothetical batoid fish, the effect of various nondimensional frequencies is studied at an aspect ratio of 1. The study is done at a maximum nondimensional amplitude of 0.15 of the pitching/undulation and a Reynolds number of 10 000. A 3D vortex structure demonstrates a spanwise symmetric double row of vortex structure at the various wavelengths while a larger wavelength also results in a horseshoe type of vortices with multiple vortex rings. For propulsive performance, the maximum thrust force (propulsive efficiency) is obtained at an intermediate (smaller) wavelength. Further, with increasing aspect ratio, an increase in the thrust force and the propulsive efficiency are found for various wavelengths. A single-row (double-row) vortex structure leading to smaller (larger) thrust force is obtained at a smaller (larger) nondimensional frequency. Using the more realistic 3D kinematics, as compared to the 2D kinematics used earlier, more realistic flow structures and the associated propulsive performance parameters are presented that can be used for the efficient design of underwater vehicles.

I. INTRODUCTION

Fishlike locomotion has been of interest to fluid dynamicists due to its surprisingly large efficiency as compared to conventional aquatic propulsion systems. Various fish use different techniques for swimming leading to various propulsion conditions. Thus, hydrodynamic analysis of various types of fishlike locomotion could lead to the efficient design of *autonomous underwater vehicles (AUV)* operating under different conditions.

Most of the fish use their *body and/or caudal fin (BCF)* motion for the propulsion. The BCF types of fish are classified into three major categories: anguilliform, carangiform, and thunniform [1]. Among the two extreme categories of fish, the anguilliform (thunniform) fish use an undulating (pitching) based motion—of their body (caudal fin)—leading to a smaller (larger) thrust force and larger (smaller) propulsive efficiency [2]. For the BCF types of fish, the kinematics and flow patterns are mostly two-dimensional. There is another category of fish, called *batoid* fish, that use batlike

---

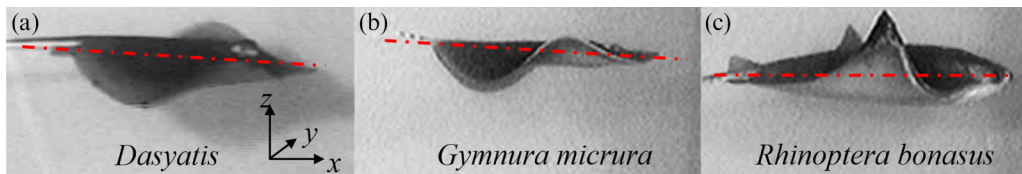*Corresponding author: atulsharma@iitb.ac.in

FIG. 1. Three different types of batoid fish, with vertical (z-direction) undulation and/or pitching motion of the body along the streamwise (x) direction and vertical (z) pitching motion of the body along the spanwise (y) direction (modified from the figure presented by Rosenberger [4]). The red lines show the center of the body ($y = 0$).

flapping (two-sided symmetric pitching) as well as the undulation of their pectoral fin for propulsion. The undulation and pitching are in different planes [3], which leads to three-dimensional (3D) kinematics and results in a large propulsive efficiency, as well as thrust generation, for the batoid fish.

Based on the difference in the *muscles-induced chordwise flexibility*, represented by a wavelength λ of a streamwise traveling wavy motion along the body, batoid fishs are classified into three major categories: *Dasyatis*, *Gymnura micrura*, and *Rhinoptera bonasus* (Fig. 1). The ratio of the wavelength λ and the chord length c (of the hydrofoil-shaped frontal cross section of the body) is $\lambda/c < 1$ for the *Dasyatis* type of fish while $\lambda/c \approx 4$ *for Rhinoptera bonasus* [4]; and *Gymnura micrura* have an intermediate value of λ/c. Thus, for a 3D kinematics-based unified study involving all the types of real and hypothetical batoid fish, the λ/c can be considered as a kinematics modeling parameter, with its larger value asymptoting to a pitching motion of the hydrofoil sections along with that of the pectoral fin.

Rosenberger and Westneat [3] analyzed the kinematics of various types of batoid fish. Rosenberger [4] classified the batoid fish based on undulatory and pitching kinematics. They considered the kinematics as a continuum, where the extreme cases have pure undulatory and pure pitching motions. Using the different kinematics, studies on the hydrodynamic analysis of the 3D fishlike locomotion can be categorized into two types: *pitching and/or heaving hydrofoils/plates* and *batoid fishlike body and kinematics*.

For a *pitching and heaving finite span hydrofoil*, von Ellenrieder *et al.* [5] experimentally studied the effect of frequency of pitching/heaving on the flow structure and compared the vortex structure formed from the leading and trailing edge vortices. Buchholz and Smits [6] conducted experimental studies on pitching panels and studied the interaction of alternatively shed horseshoe vortices. With increasing frequency of pitching, their later study [7] reported an additional vortex structure that appears due to the expansion of streamwise vortices. Green *et al.* [8] experimentally studied the hydrodynamics of a trapezoidal pitching panel and found that the complexity of vortex structure is more at a larger frequency, due to the spreading of spanwise vortices in the vertical direction. From a similar study, King *et al.* [9] found alternatively interacting vortices for all the frequencies. Bi and Cai [10] presented an experimental study on a spanwise flexible pitching hydrofoil and concluded that moderate flexibility leads to a larger thrust force while the larger flexibility leads to a larger propulsive efficiency. Li and Dong [11] numerically studied the hydrodynamics of a pitching plate and found that interconnected C-shaped vortex rings result in a bifurcating wake pattern. Hemmati *et al.* [12] numerically studied the effect of trailing edge shape on the vorticity dynamics of a pitching panel and found that a concave trailing edge shape results in strong 3D effects.

For a *batoid fishlike undulating fin*, Clark and Smits [13] experimentally studied the 3D flow structure for a various frequency of undulation. Moored *et al.* [14] conducted an experimental study on the hydrodynamics of a flapping fin, inspired from the pitching batoid fish, and found that pitching as compared to undulation produces an entirely different flow structure due to the formation of leading-edge vortices. Chen *et al.* [15] developed a mathematical model for the 3D undulating

TABLE I. Body shape, kinematics, Reynolds number Re ($\equiv \rho u_\infty c/\mu$), nondimensional wavelength λ^*, and aspect ratio A_R, considered in the published literature and present work, for hydrodynamic study on batoid fishlike locomotion. All the studies are experimental, except the last three.

Reference	Body shape	Kinematics	Re	λ^*	A_R
Clark and Smits [13]	Ellipsoid	Undulation	11400	1.0	1.83
Moored et al. [14]	Robotic fin	Pitching	548–74000	∞	
Dewey et al. [16]	Ellipsoid	2D unified	8100–11600	2.4–∞	0.9
Moored et al. [17]		kinematics	11600	2.4–∞	0.9
Chen et al. [15]	Batoid	Undulation		1.0	1.0
osilevskii [18]	Plate			1.0	
Bottom et al. [19]	Batoid		13500–23000	0.83	1.0
Present	Ellpisoid	3D unified kinematics	10000	0.8–∞	0.5–1.0

batoid kinematics. Dewey et al. [16] experimentally studied the hydrodynamics of batoid fishlike undulating elliptical hydrofoil and reported a transition from periodic shedding of a single vortex to a pair of vortices per cycle of undulation, with decreasing the wavelength of undulation. Moored et al. [17] conducted a stability analysis on a batoid fishlike pitching fin and concluded that the maximum propulsive efficiency is obtained when the frequency of pitching becomes equal to the resonance frequency of the jet profile behind the fin. Iosilevskii [18] used a strip theory to study the hydrodynamics of a batoid fishlike undulating plate and found that the propulsive efficiency is independent of the aspect ratio of the plate. Bottom et al. [19] numerically studied the self-propelled motion of a batoid stingray, modeled from the experimental measurements of real stingray, and concluded that fast stingrays are efficient.

For hydrodynamic analysis of batoid fishlike locomotion, a summary of the literature survey as well as our work is presented in Table I. The table shows that the studies are for either streamwise undulating or streamwise pitching and for a unified kinematics (involving a transition from undulating to pitching with increasing λ) of an actual or approximated (by ellipsoid) shape of the batoid fish. However, the present work considers a more realistic 3D unified kinematics as compared to the 2D unified kinematics considered by Dewey et al. [16] and Moored et al. [17]. The present study also considers a two-sided symmetric-pitching motion (batlike flapping) about a midplane along with the 2D unified kinematics (involving a traveling-wave motion in the streamwise direction that corresponds to the undulation asymptoting to pitching at larger λ), considered by the previous researchers [16,17]. Furthermore, the table shows that the present work considers a much wider range of the muscles-induced chordwise flexibility λ^* (= 0.8, 1.2, 4, and ∞) for the unified kinematics and aspect ratio A_R (= 0.5, 0.75, and 1.0) of the spanwise elliptical shape of batoid fish. Thus, using the 3D unified-kinematics model, the objective of the present three-dimensional work is to study the effect of λ^*, aspect ratio A_R, and nondimensional frequency St of the periodic 3D kinematics on the hydrodynamic characteristics and propulsive performance of the 3D batoid fishlike locomotion at dynamic steady state. The locomotion considered here corresponds to constant velocity propulsion, called tethered propulsion, and is modeled here by considering a free-stream flow across an undulating/pitching batoid fishlike undulating body. The free-stream flow is also considered by all the published literature presented in Table I, except the study by Chen et al. [15], which is on self-propelled simulation.

II. KINEMATICS AND COMPUTATIONAL MODEL

A. 3D unified-kinematics model for various types of batoid fishlike locomotion

Most of the batoid fish have more or less a hydrofoil-shaped frontal cross section with an elliptical span [3,4] (considered here and shown in Fig. 2). The figure shows a batoid fishlike 3D body along
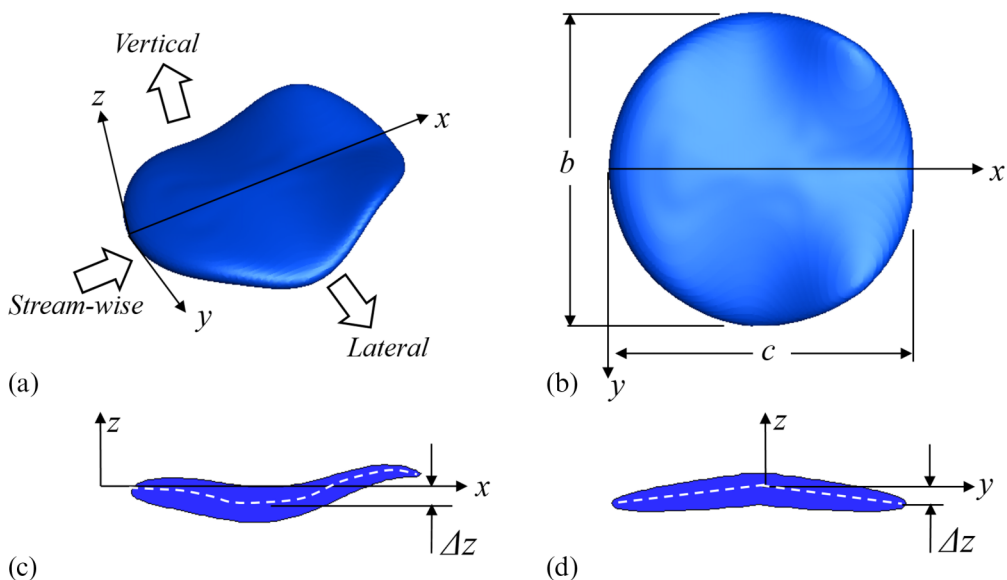
FIG. 2. Batoid fishlike body: (a) 3D view, and (b)–(d) various 2D views: (b) top view, (c) front cross-sectional view (at $y = 0.25b$), and (c) side cross-sectional view (at $x = 0.5c$) of the batoidlike body.

with various 2D views. The top view in Fig. 2(b) shows an ellipse with the length of the major and minor axes as c and b, respectively. A cross-sectional front view in Fig. 2(c) shows a NACA0012 hydrofoil, with a chord length of c at the spanwise midplane ($y = 0$); note that the chord length $c(y)$ reduces from the midplane along the elliptical spanwise direction ($0 < y < \pm b/2$). A cross-sectional side view in Fig. 2(d) shows the streamwise cross section as a two-sided inclined plate, corresponding to a decreasing thickness of the NACA0012 hydrofoil from the midplane $y = 0$ to the edge of the ellipsoid $y = \pm b/2$. A parametric representation of the geometry is given as

$$z(x, y) = z_t(x)\sqrt{1 - \frac{y^2}{[b(x)]^2}} \quad \text{where}$$

$$z_t(x) = 0.178\,14\sqrt{x} - 0.0756x - 0.210\,96x^2 + 0.170\,58x^3 - 0.0609x^4$$

$$\text{and} \quad b(x) = b/2\sqrt{1 - \frac{(x - c/2)^2}{(c/2)^2}}. \tag{1}$$

For the various types of batoid fish shown in Fig. 1, the streamwise line along the midplane $y = 0$ of the body (represented by a red arrow in Fig. 1) is almost stationary, and the hydrofoil cross section (of the pectoral fins) on both the sides of the midplane undergoes a streamwise wavy undulating motion [3]. Thus, the vertical amplitude of the wavy motion is zero at the centerline and maximum at the tip of the pectoral fin. There is an almost linear variation of the amplitude from the body centerline $y = 0$ to the tip of the fin $y = \pm b/2$. This variation of amplitude is due to a batlike flapping (two-sided pitching motion) in the streamwise y-z plane. Thus, the kinematics is a combination of the wavy motion (of the hydrofoil cross section) in the lateral x-z plane and the two-sided pitching motion (of the elliptical cross section) in the streamwise y-z plane. For the present 3D unified-kinematics model, the hydrofoil cross sections are subjected to a 2D unified kinematics proposed in our recent study for 2D hydrofoils [2] while the streamwise cross section is subjected to the two-sided flappinglike pitching motion.

Although the kinematics considered here for various types of batoid fish has been reported in the literature [3,4], here we propose a 3D mathematical model for the kinematics, as a combination of pitching and undulating motion. Further, we unified the kinematic model for the various types of batoid fishlike body and kinematics, by varying the wavelength of undulation (streamwise) and aspect ratio of the body. The present 3D unified kinematics is proposed as a combination of 2D unified kinematics (proposed in our recent work [2]) for the hydrofoil cross sections and pitching motion of the streamwise cross section. The combination of the 2D unified kinematics and the flappinglike two-sided symmetric-pitching motions is represented by a nondimensional form of a 3D unified-kinematics model, for the vertical displacement $\Delta Z = \Delta z/c$ [of the ellipsoidal x-y plane; refer to Figs. 2(c) and 2(d) for Δz], given as

$$\Delta Z = \frac{A_{\max} X |Y|}{0.5 A_R} \sin\left[2\pi \left(\frac{X}{\lambda^*} - \frac{St\tau}{2A_{\max}} \right) \right] \quad \text{where } X = [0, 1], \quad Y = [-0.5A_R, 0.5A_R], \quad (2)$$

$X = x/c$, $Y = y/c$, τ is the nondimensional time ($\equiv t u_\infty/c$), and A_R ($\equiv b/c$) is the aspect ratio of the body. Furthermore, St ($\equiv 2f a_{\max}/u_\infty$), $A_{\max}$ ($\equiv a_{\max}/c$), and λ^* ($\equiv \lambda/c$) are the nondimensional frequency, amplitude, and wavelength of undulation, respectively. Here, $a_{\max}$ is the maximum amplitude of undulation for the hydrofoil cross section at $y = \pm b/2$. The $a_{\max}$ also corresponds to the amplitude for the two-sided pitching motion. Furthermore, λ is the wavelength and f is the frequency of undulation of the 2D hydrofoil cross section. Note that the undulating and pitching motions are in the vertical direction z for the batoid fish as compared to the lateral direction y in the BCF type of fish.

For the 3D unified kinematics proposed above [Eq. (2)], $\lambda^* < 1$, intermediate value of λ^*, and larger λ^* correspond to the *Dasyatis, Gymnura micrura,* and *Rhinoptera bonasus* type of batoid fish, respectively (Fig. 1). Thus, the proposed 3D unified kinematics covers the various types of batoid fishlike locomotion.

B. Computational model

The nondimensional computational setup for the batoid fish in a free-stream flow, corresponding to the tethered propulsion, is shown in Fig. 3. The figure shows the nondimensional computational domain along with boundary conditions applied at the various faces of the computational domain. A constant free-stream velocity u_∞ based boundary condition is applied at the inlet, and the outflow boundary condition is applied at the outlet. The no-slip boundary condition is applied on the body surface, whereas the free-slip boundary condition is applied on the external (top, bottom, left, and right) boundaries. The mathematical description of the various boundary conditions is included in Fig. 3.

III. NUMERICAL DETAILS

A level-set function based immersed interface method (LS-IIM), recently proposed by us [20] for a 2D problem, is extended here for the present 3D problem. The LS-IIM considers the Eulerian description and finite volume method for the fluid dynamics, and the Lagrangian description and finite element method for the structure dynamics. The fluid flow is solved using a fully implicit pressure projection method on a colocated Cartesian grid [21]. The fluid-structure interface is traced using a level-set function obtained from a geometric method (minimum distance and winding number algorithm). The LS-IIM involves a direct application of the boundary conditions at the interface, using the level-set function. The LS-IIM based in-house 3D code is parallelized using the message Passing interface (MPI).

A verification, as well as validation, study of the present LS-IIM can be found in Thekkethil and Sharma [20], for various 2D fluid-structure interaction (FSI) problems. However, for the present 3D FSI problem, a verification study of the LS-IIM is done for 3D problems of varying complexities. Firstly, the code is verified for a 3D lid-driven cavity flow problem and also for a free-stream flow
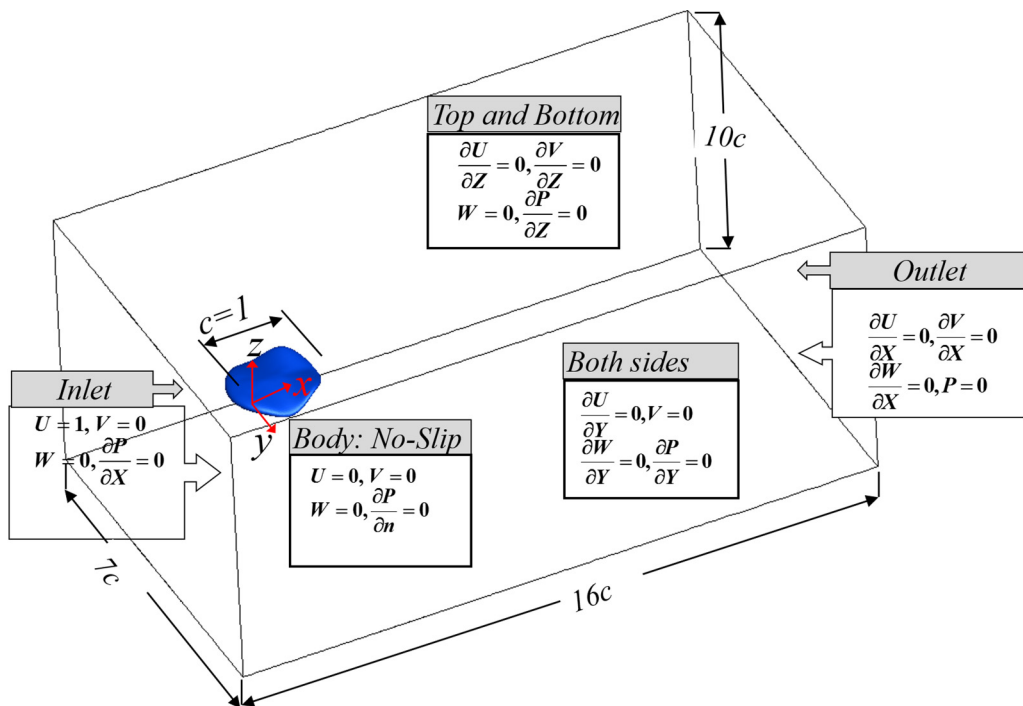
FIG. 3. Nondimensional computational setup for the tethered propulsion of batoid fishlike body and kinematics. The hydrofoil-shaped frontal cross sections are undulating with a chordwise flexibility of λ^* and the aspect ratio of the ellipse-shaped top cross section is A_R. The nondimensional frequency of the undulation of the frontal cross section and two-sided symmetric-pitching motion of the streamwise cross section is St while the nondimensional amplitude of the undulation/pitching is $A_{\max}$.

across a stationary sphere at a Reynolds number of 50 [22]. For the latter problem, a good agreement is found between the present results and that reported by Johnson and Patel [23], with an error of 4.5% for the mean drag coefficient. Thereafter, the 3D code verification is done for a free-stream flow across a pitching and heaving ellipsoid at Reynolds number Re = 200, maximum pitching angle $\theta_{\max} = 30°$, nondimensional heaving amplitude $h_{\max} = 0.5$, and Strouhal number St = 0.6. Note that the domain size ($16 \times 15 \times 15$), the grid size (smaller grid size of $\delta = 0.005$), and the time step (2000 time steps in one cycle of pitching and heaving) used for the verification study are almost the same as that used by Dong *et al.* [24]. Good agreement between the present results and that reported by Dong *et al.* [24] are presented in Fig. 4, for 3D vortex topology; and in Table II, for C_{Dm} as well as C_{Lrms}. The slight difference between the results may be due to the difference in the order of accuracy of both the numerical methods; our method is second-order accurate in space and

TABLE II. Comparison of mean drag coefficient C_{Dm} and the rms value of lift coefficient C_{Lrms}, obtained by the present simulation and that reported by Dong *et al.* [24], for a pitching and heaving ellipsoid at a Reynolds number Re = 200, pitching amplitude $\theta_{\max} = 30°$, heaving amplitude $h_{\max} = 0.5$, aspect ratio $A_R = 1.27$, and Strouhal number St = 0.6.

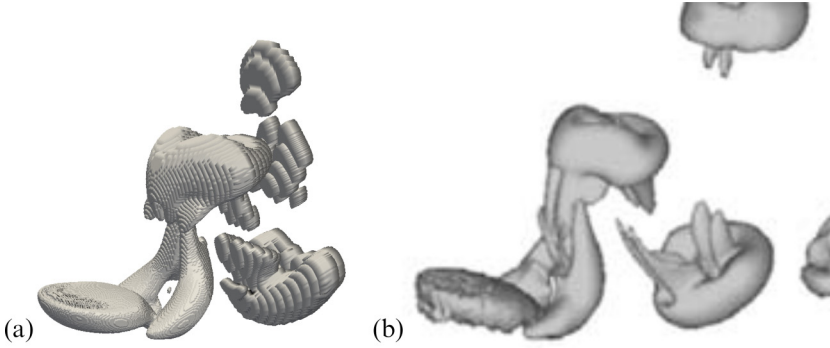|	Present study	Dong *et al.* [24]	% Error
C_{Dm}	0.234	0.251	6.77
C_{Lrms}	2.828	2.947	4.04

FIG. 4. Vortex topology from (a) present study and (b) Dong *et al.* [24], for a pitching as well as heaving ellipsoid at Re = 200, pitching amplitude $\theta_{max} = 30°$, heaving amplitude $h_{max} = 0.5$, and Strouhal number St = 0.6.

first-order accurate in time [20], whereas the method reported in Dong *et al.* [24] is second-order accurate in both space and time.

Further, for a larger Re = 2857, our simulation results are compared with that of Kern and Koumoutsakos [25], for a 3D anguilliform fishlike body and kinematics, at $\lambda^* = 1.0$, St = 0.75, and $A_{max} = 0.16$. The simulations are conducted at almost the same domain size, grid size (finer grid size $\delta = 0.003$ near the body), and time step (200 time steps in one undulation cycle), used in the literature. Figure 5 shows excellent agreement between the present results and the published results for the temporal variation of C_D, with the amplitude of C_{Dmax} as 0.026 in the present and 0.03 in the published work. The detailed verification exercises provide confidence in the results obtained from the present code.

Based on our experience from previous 2D simulations [2,20,26] and literature [24], a nondimensional domain size of $16 \times 7 \times 10$ (Fig. 3) and a nondimensional time step of 400 time steps for one cycle of undulation are considered in the present study. Similar undulation cycle based selection of time step was reported in the literature [24,25]. To ensure that the domain size and time step are
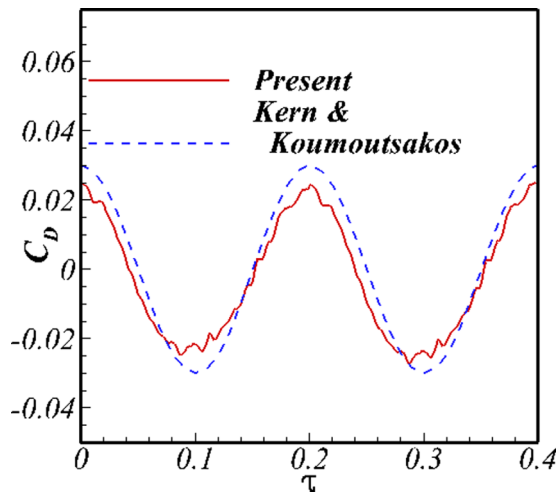

FIG. 5. For a 3D anguilliform fishlike body and kinematics, comparison of present and published results [25] for temporal variation in the drag coefficient C_D, at $\lambda^* = 1.0$, St = 0.75, Re = 2857, and $A_{max} = 0.16$.
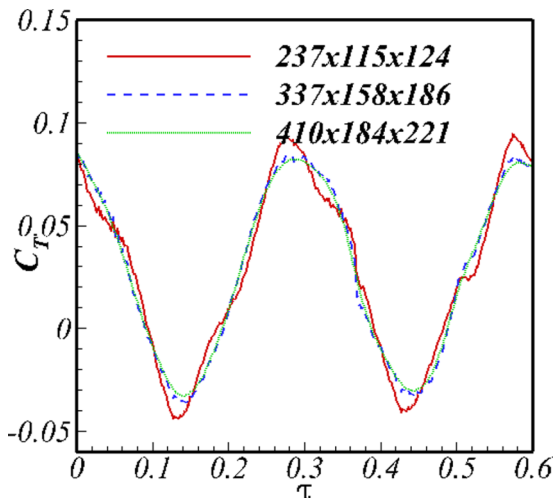
FIG. 6. Temporal variation in instantaneous thrust force coefficient C_T for three different grid sizes, at $\lambda^* = 4.0$, $A_R = 1.0$, St $= 0.5$, $A_{max} = 0.15$, and Re $= 10\,000$.

sufficient enough to result in accurate solutions, 3D simulations are done at a larger domain size $25 \times 10 \times 15$ and a smaller time step of 800 times steps per undulation cycle, at $\lambda^* = 4.0$, $A_R = 1.0$, St $= 0.5$, $A_{max} = 0.15$, and Re $= 10\,000$. The resulting mean thrust coefficient $C_{Tm} = 0.0284$ for the larger domain and $C_{Tm} = 0.0279$ for the smaller time step are almost the same (less than 1% error) as that of $C_{Tm} = 0.0282$ obtained for the domain and time step considered here. Furthermore, the maximum value of viscous stress on the body is found to be almost the same (0.0140 and 0.0141), with the decreasing time step.

Further, for a grid independence study, 3D simulations are done at $\lambda^* = 4.0$, $A_R = 1.0$, St $= 0.5$, $A_{max} = 0.15$, and Re $= 10\,000$ for three nonuniform Cartesian grid sizes: $237 \times 115 \times 124$, $337 \times 158 \times 186$, and $410 \times 184 \times 221$. Figure 6 shows almost the same temporal variation of C_T for the last two grid sizes; and the maximum value of viscous stress on the body is found to be 0.0149, 0.0140, and 0.0139, for the respective grid size. Thus, the intermediate grid size of $337 \times 158 \times 186$ is considered sufficient for the grid independent results and used for the present 3D simulations. Further, for the three grid sizes considered here, the finest grid sizes are $\delta = 0.015$, 0.01, and 0.008; and the coarsest grid sizes are $\Delta = 0.5$, 0.25, and 0.125. A uniform finest grid δ is used in a region near the body where the movement of the body is restricted, and a uniform coarsest grid Δ is used far away from the body. A hyperbolic stretching is used in the region between the finest and coarsest grids.

IV. 3D UNIFIED-KINEMATICS BASED STUDY ON VARIOUS TYPES OF BATOID FISHLIKE LOCOMOTION

For the present 3D biological flow problem, the various nondimensional input as well as output parameters considered here and an introduction of the various 3D vortex structures encountered are presented in separate sections below.

A. Parametric details

For the tethered simulation of various types of batoid fishlike body and kinematics, a detailed parametric study is done for various nondimensional wavelengths λ^* (of undulation of the hydrofoil cross section), aspect ratio A_R (of the spanwise elliptical cross section), and Strouhal number St (nondimensional frequency of undulation/pitching) at a constant Reynolds number Re $= 10\,000$

and nondimensional maximum amplitude of undulation/pitching $A_{\max} = 0.15$. In this regard, the nondimensional parameters considered are as follows:

Effect of λ^* and A_R:

$\lambda^* = 0.8,\ 1.2,\ 4.0,\ \text{and}\ \infty$	at St $= 0.5$, Re $= 10\,000$, and $A_{\max} = 0.15$
$A_R = 0.5,\ 0.75,\ \text{and}\ 1.0$	

Effect of St:

St $= 0.2,\ 0.5,\ \text{and}\ 0.7$	at $\lambda^* = 0.8$ and ∞, $A_R = 1.0$, Re $= 10\,000$, and $A_{\max} = 0.15$

Thus, the effect of λ^*, A_R, and St on the flow pattern and propulsive performance parameters are studied. The smaller, intermediate, and larger λ^* corresponds to *Dasyatis sabina*, *Gymnura micrura*, and *Rhinoptera bonasus* types of batoid fish, respectively [4]. Further, *Rhinobatos lentiginosus* and *Raja eglanteria* (Fig. 1) types of batoid fish have a smaller aspect ratio as compared to *Gymnura micrura* and *Rhinoptera bonasus*. Thus, the kinematics model proposed in this work considers almost all the types of batoidlike locomotions. From a literature survey conducted by Rosenberger [4] on different types of batoid fish, a smaller nondimensional wavelength $\lambda^* \approx 0.8$ was found for an undulatory batoid fish *Dasyatis sabina*; and a larger wavelength $\lambda^* \approx 4.0$ was found for *Rhinoptera bonasus* type of batoid fish. Thus, in our study, the smallest, intermediate, and larger wavelengths considered are 0.8, 1.2, and 4.0, respectively. We also considered $\lambda^* = \infty$, where the kinematics is purely based on pitching motion, to study the effect of the absence of the wavy motion (as compared to both wavy and pitching motions at the smaller λ^*) on the batoidlike locomotion. In this study, the aspect ratio A_R is varied from 0.5 to 1.0, which is close to the real batoid fish (Rosenberger [4]). Rosenberger [4] reported that most of the batoid fish swim in the range of a Strouhal number of 0.2–0.7, considered above in our parametric study. The study is conducted at a constant maximum amplitude $A_{\max} = 0.15$, which is within the range of $A_{\max}$ used by the various types of batoid fish [4].

A constant Reynolds number of Re $= 10\,000$ is considered here that corresponds to the larger value of Re considered by the previous researchers for the present problem (Table I). A literature survey based scaling analysis for real fish locomotion by Gazzola *et al.* [27] reported that the Reynolds number for the various fish varies from Re $= 10^3$ to 10^7 (depending on the geometrical and kinematic parameters of the fish), with the transition from laminar to turbulent flow at around Re $= 10^4$. Further, for a tunalike body and kinematics, Chang *et al.* [28] compared the flow structure and propulsive performance parameters obtained from the laminar and turbulent simulations for three Reynolds numbers: Re $= 7.1 \times 10^3$, 7.1×10^4, and 7.1×10^5. For the respective Re's, they reported negligible, close to 10%, and considerable difference in their results with and without a turbulence model. Thus, the present 3D simulations at Re $= 10^4$ is either in laminar or in transitional flow regime; and simulated here without using any turbulence model.

For the batoid fishlike locomotion, the various nondimensional propulsive performance parameters are thrust force coefficient C_T, lift force coefficient C_L, and propulsive efficiency η_P, defined as follows:

$$C_T = \frac{F_T}{{}^1\!/_2 \rho_f u_\infty^2 A_s}, \qquad C_L = \frac{F_L}{{}^1\!/_2 \rho_f u_\infty^2 A_s},$$

$$\eta_P = \frac{P_{\text{out},m}}{P_{\text{in},m}} = \frac{F_{Tm} u_p}{\int f_L . v_{\text{body}} ds} = \frac{C_{Tm}}{\int c_{Tr} . V_{\text{body}} dS}, \tag{3}$$

where F_T is the thrust force, F_L is the lift force, and A_s the spanwise area of the foil. The definition of η_P is similar to our recent 2D study [2], except that the lateral force in the 2D study for BCF fish is replaced with the vertical force for the present batoid fish.
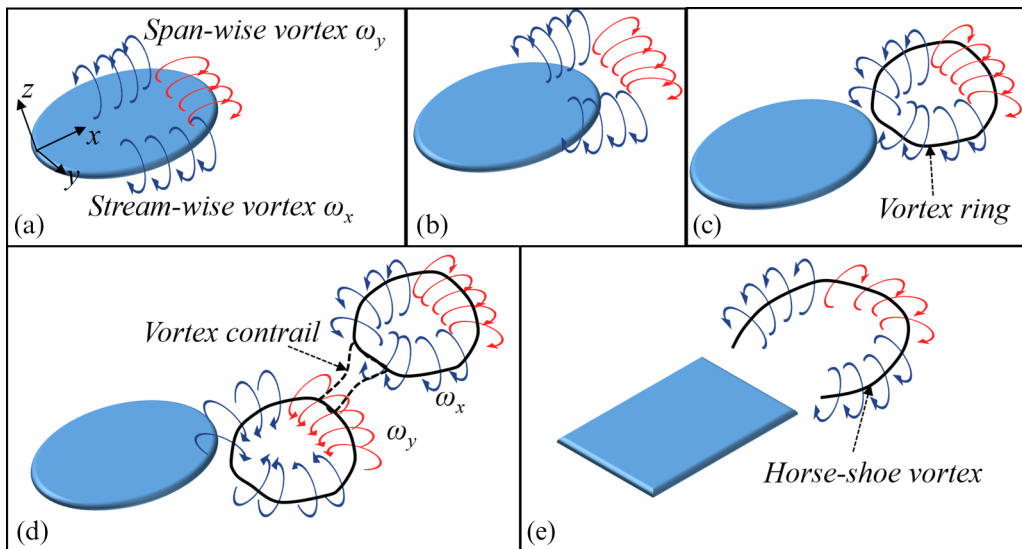
FIG. 7. Schematic representation of the formation of vortex ring, vortex contrail, and horseshoe vortex from a 3D body oscillating in the vertical direction (z direction). Formation of spanwise (streamwise) vortices on the trailing edge (sides) of the body is shown in (a). The spanwise and streamwise vortices together form a vortex ring, shown in (c); and a vortex contrail is formed between the two vortex rings [shown in (d)]. When the streamwise vortices are farther apart at the trailing edge, a horseshoe vortex is formed instead of the vortex ring as shown in (e).

B. Introduction to three-dimensional vortex structures

Three-dimensional vortex structures are presented, in the present work, using the Q criterion [29], given as

$$Q = \tfrac{1}{2}[\mathrm{tr}(\bar{D})^2 - \mathrm{tr}(\bar{D}^2)], \qquad (4)$$

where $\bar{D}$ is the velocity gradient tensor. A contour of $Q = 0$ is plotted to represent the Q-criterion based 3D vortex structure, presented below. Before presenting a Q-criterion based 3D vortex structure for the present 3D FSI problem, an introduction of the various terminology involved in a discussion of a 3D vortex structure is presented here, with the help of Fig. 7.

The periodic 3D kinematics of the batoid fishlike body results in various types of 3D vortex structure behind the body. The 3D vortex structure is a combination of *vortex rings*, *vortex contrails*, and *horseshoe vortex*, shown schematically in Fig. 7 for flow across an oscillating (pitching and/or heaving) 3D body. The oscillation results in spanwise (y) vortices with vorticity ω_y at the trailing edge of the body, represented by red arrows in Fig. 7(a). These vortices are similar to that found from 2D simulation for flow across a body oscillating in the x-z plane. In 3D, in addition to the spanwise vorticity ω_y, streamwise vortices with vorticity ω_x are formed on the sides of the body [represented by blue arrows in Fig. 7(a)]. When the spanwise, as well as streamwise vortices, advect downstream, they come close to each other as shown in Fig. 7(b). If the body shape is spanwise tapered at the trailing edge (such as spanwise elliptical shape considered in this study), the downstream advection of these vortices results in movement of these vortices towards each other and forms a complete loop as shown in Fig. 7(c) −, called a *vortex ring* [24]. A similar vortex ring is formed in the other half-cycle of the oscillation, also as shown in Fig. 7(d). The streamwise vortices ω_x from the first half-cycle and spanwise vortices ω_y from the second half-cycle have the same sense of rotation. Thus, a stretched vortex is formed between the two vortex rings as shown in Fig. 7(d), called a *vortex contrail* [24]. If the trailing edge of the body is not tapered, as in the case of a rectangular
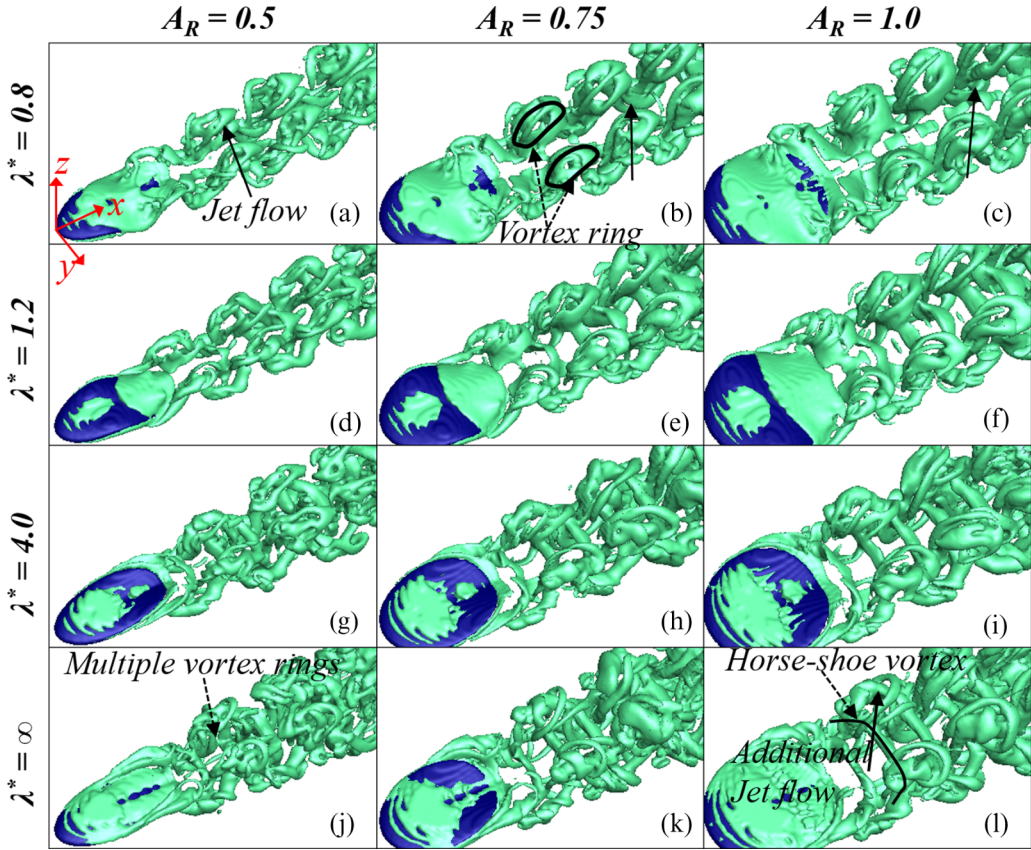
FIG. 8. Effect of λ^* and A_R on the instantaneous Q-criterion based 3D vortex structure, for the batoid fishlike body, kinematics, and tethered propulsion, at Re = 10 000. The hydrofoil-shaped frontal cross sections are undulating with various chordwise flexibilities λ^* and aspect ratio of the spanwise elliptical cross section A_R. The nondimensional frequency of the undulation of the frontal cross section and the two-sided symmetric-pitching motion of the streamwise cross section is St = 0.5 while the maximum nondimensional amplitude of the undulation/pitching is $A_{\max} = 0.15$. Note that the time instant shown in the figures correspond to the starting of the undulating/pitching cycle, i.e., $\tau = 0$; and the tail position varies with λ^* at $\tau = 0$.

pitching plate [Fig. 7(e)], the streamwise vortices formed on the edges are unable to join and do not form a loop or vortex ring, resulting in a vortex structure of horseshoe shape, called a *horseshoe vortex* [5], shown in Fig. 7(e).

V. EFFECT OF CHORDWISE FLEXIBILITY AT THE HYDROFOIL CROSS SECTION AND ASPECT RATIO OF THE SPANWISE ELLIPSE

A. Instantaneous flow pattern

The effect of the chordwise flexibility λ^* and the aspect ratio A_R on the instantaneous flow pattern is shown in Fig. 8 for the 3D vortex structure; and 2D contours (on a vertical plane at $Y = 0.25A_R$) are shown in Figs. 9 and 10 for spanwise vorticity ω_y and streamwise velocity U, respectively.

As compared to the single pair of vortex rings [shown schematically in Fig. 7(d)] that was reported earlier for pitching and heaving hydrofoil [24] as well as an anguilliform fishlike undulating body [25], a double pair of vortex rings is seen in Fig. 8 for smaller λ^* (0.8 and 1.2) and all the values of A_R studied here. The figure shows each pair of rings connected by the vortex contrail on the front
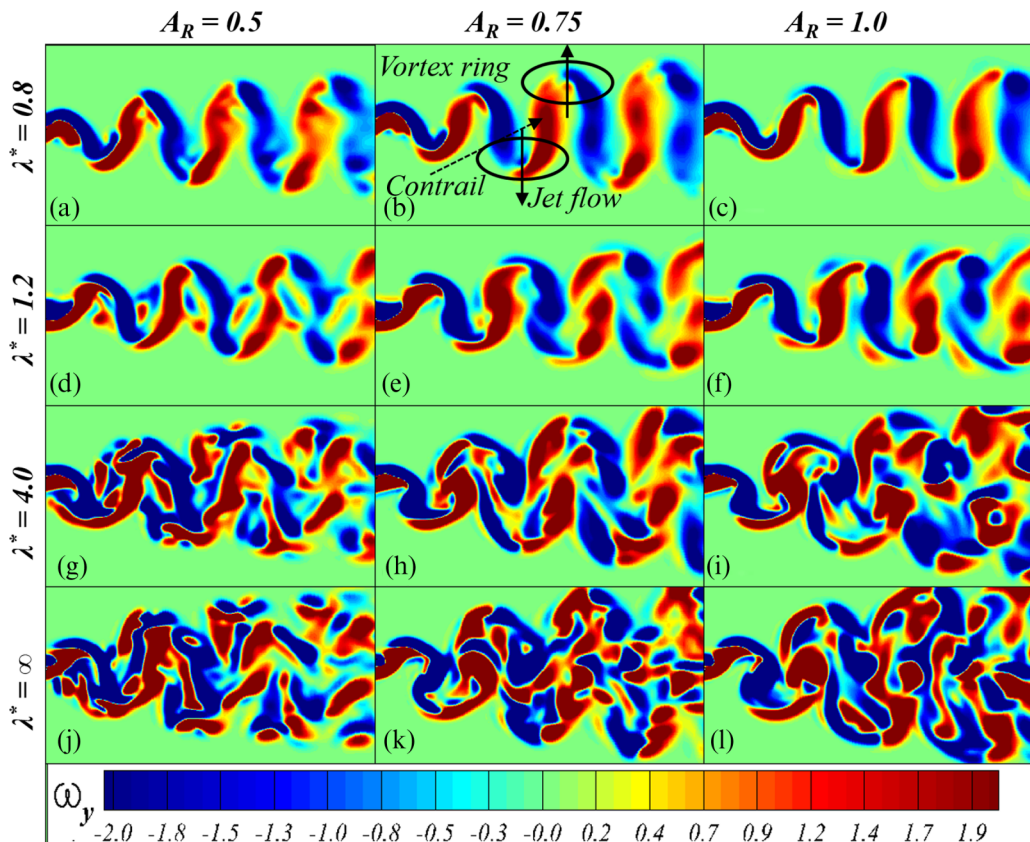
FIG. 9. Effect of nondimensional chordwise flexibility λ^* and aspect ratio A_R on the instantaneous spanwise vorticity (ω_y) contours (at $Y = 0.25A_R$), for the batoid fishlike locomotion, at St = 0.5, $A_{max} = 0.15$, and Re = 10 000.

and back sides. A similar result was also reported by Fish *et al.* [30] for Manta fish. Further, the vortex rings formed are not as smooth as compared to that by Dong *et al.* [24]. This could be due to the larger Reynolds number considered in the present study. The two vortex rings [marked in Fig. 8(b)] are formed due to the two-sided symmetric-pitching motion (on both sides of the plane of symmetry), leading to two sets of streamwise vortices; one on the sides and the other on the plane of symmetry. The mechanism of formation of the vortex rings is discussed later in Sec. VII A.

For the larger wavelength ($\lambda^* = \infty$) at all A_R, a horseshoe vortex structure [marked in Fig. 8(l)] with a complicated 3D vortex structure is seen in Figs. 8(j)–8(l). This horseshoe vortex was also reported earlier for a pitching and heaving plate by von Ellenrieder *et al.* [5]. Further, for a constant λ^*, a reduction in the lateral spacing between the pair of vortex rings with decreasing A_R results in the reduction of the strength of the vortex and a jet flow [marked in Fig. 8(a)] which is inclined upstream of the free-stream flow in Fig. 8(a) and downstream from the flow in Figs. 8(b) and 8(c), and thus results in a reduction in the net thrust force coefficient with decreasing A_R (presented later). For larger A_R [Fig. 8(c)], since the trailing edge spanwise vortex forms over a larger span, it splits and multiple vortex ring formation starts. A smoother vortex ring formation is obtained for intermediate A_R [Fig. 8(b)]. For all the flexibilities λ^*, Fig. 8 shows that the complexity of the 3D vortex structure is more at the smallest A_R. This is because the trailing edge spanwise vortex becomes almost insignificant as compared to the streamwise vortices.
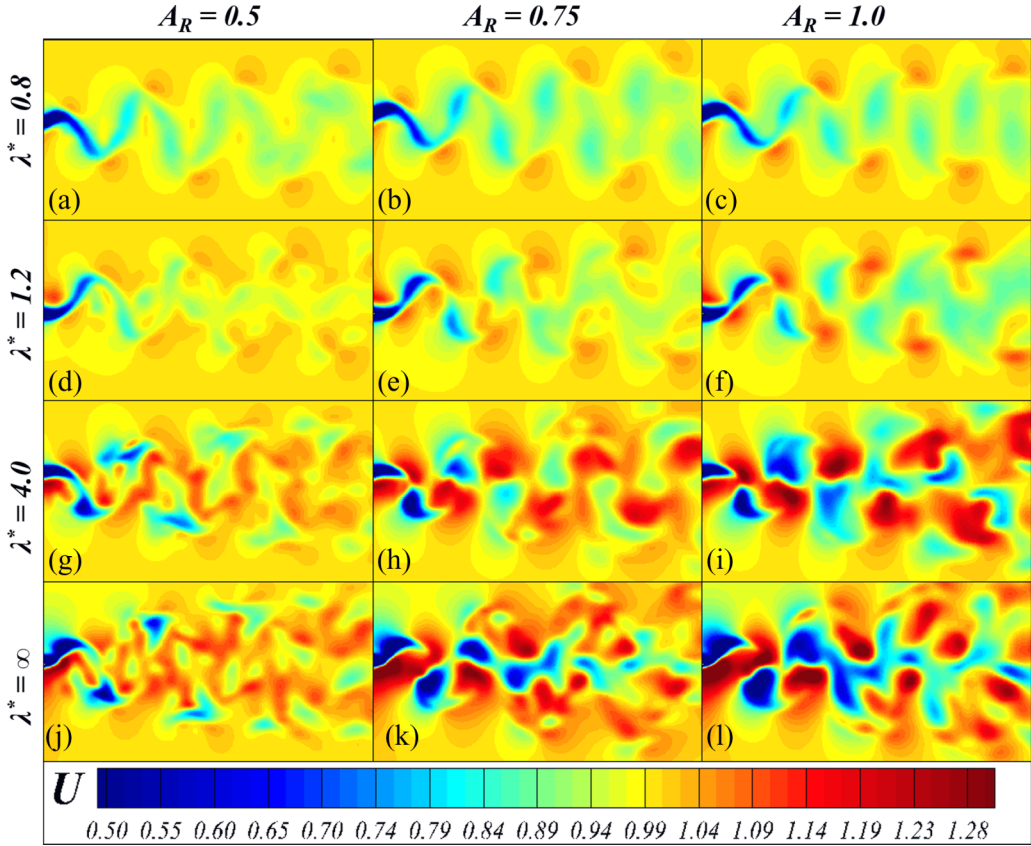
FIG. 10. Effect of nondimensional chordwise flexibility λ^* and aspect ratio A_R on the instantaneous streamwise velocity (U) contours (at $Y = 0.25A_R$), for the batoid fishlike locomotion, at St $= 0.5$, $A_{\max} = 0.15$, and Re $= 10\,000$.

With increasing λ^*, the figure shows the appearance of the horseshoe vortex, and maximum strength of the horseshoe vortex is obtained for the larger λ^* [Figs. 8(j)–8(l)]. The horseshoe vortex results in an additional jet flow formation [Fig. 8(l)] resulting in an enhancement in the hydrodynamic force coefficients. Also, with increasing λ^*, the phase difference between pitching motion in the y-z plane and undulating motion in the x-z plane decreases (explained later in Sec. VII A). Thus, the interaction between the streamwise vortices from two half-cycles results in the formation of a complex vortex ring for larger λ^*; whereas, a properly directed streamwise vortex results in a smoother ring formation for smaller λ^*. The complexity of vortex rings increases with increasing λ^*. Figures 8(d)–8(f) show both horseshoe vortex and smoother vortex rings at $\lambda^* = 1.2$ that may result in the optimum propulsive performance condition (maximum thrust force and efficiency). Note that the combined horse-shoe vortex and vortex rings presented in Figs. 8(d)–8(i) are not found in the literature for the batoid fishlike locomotion, and are presented here as a new flow structure. For $\lambda^* = 1.2$ and $\lambda^* = 4.0$, with increasing A_R, Figs. 8(d)–8(i) show that the horseshoe vortex strength increases with an increase in A_R due to much stronger trailing edge spanwise vortices, which may lead to enhancement in propulsive performance.

For an undulating 2D NACA0012 hydrofoil, a reverse von Kármán vortex street along with a jet formation behind the foil was presented in our recent study [2]. The 2D flow structure is presented here for the 3D batoidlike undulation by a 2D contour plot, of the trailing edge spanwise vorticity

ω_y in Fig. 9 and streamwise velocity U in Fig. 10, at a plane $Y = 0.25A_R$ where the spanwise vortex strength is almost maximum. This gives a direct comparison with the 2D flow structure at various λ^* and A_R, and explains the vortex ring formation and jet flow.

The double row of vortex rings, seen in the 3D vortex structure, is marked in the 2D vorticity contours for $\lambda^* = 0.8$ [Fig. 9(b)]. The vortex ring marked on the upper side corresponds to the ring shed when the tip of the hydrofoil cross section reaches the topmost position. This vortex ring that is formed by the combination of the streamwise vortex on edges and the plane of symmetry (discussed above) is presented in Fig. 9(b) by the spanwise trailing edge vortex that is clockwise (CW) and countclockwise (CCW) on the right and left sides of the upper ring, respectively. Since the trailing edge vortex for the next cycle starts forming when the upper ring is shed, a vortex contrail of CCW sense is followed by the vortex ring and joins with the CCW trailing edge vortex of the next half-cycle [marked on the right side of the bottom ring in Fig. 9(b)]. Figure 9(b) also shows the jet flow within the upper and lower rings in the upward and downward directions, respectively. The vortex rings [Fig. 8(b)] result in two jets on both sides [Fig. 10(b)]. In the case of the 2D undulating hydrofoil, the vortex contrail is not present, and a single jet flow is formed between the CW and CCW vortices formed in two half-cycles.

With decreasing A_R for the smaller $\lambda^* = 0.8$, Figs. 9(a)–9(c) show a narrower vortex ring and a decrease in the strength of vortices. Further, with decreasing A_R, the reduction in strength of the spanwise vortices results in a decrease in the streamwise velocity and strength of the jet flow [Figs. 10(a)–10(c)]. With increasing λ^*, Fig. 9 shows multiple vortex structures that result in the formation of multiple rings. The complex spanwise vortex distribution in Figs. 9(g)–9(l) show a complex vortex structure that results in a mixed jet formation [Figs. 10(g)–10(l)] as compared to the two separate jets at smaller wavelengths [Figs. 10(a)–10(f)]. The formation of the horseshoe vortex at the larger λ^* [Fig. 8(c)] results in a stronger spanwise vorticity (Fig. 9) and a stronger jet flow at larger λ^* (Fig. 10). Further, with increasing A_R, an increase in the strength of the horseshoe vortex increases the strength of the jet. Thus, the horseshoe vortex plays a vital role in the propulsive performance at this range of λ^* and A_R.

B. Propulsive performance parameters

The above discussed 3D and 2D flow characteristics are the cause while the propulsive performance parameters are the effect in the present cause-and-effect based biological hydrodynamics analysis. This section presents the effect of λ^* and A_R on the propulsive performance parameters (C_{Tm}, C_{Lrms}, and η_p) for batoid fishlike locomotion, at St = 0.5, $Re_{u_p} = 10\,000$, and $A_{max} = 0.15$. Figure 11 shows the temporal variation of the instantaneous C_T and C_L, whereas Fig. 12 shows the time-averaged propulsive performance parameters (C_{Tm}, C_{Lrms}, η_P). Note that the time-averaging is done using the last two cycles of the simulated results, ensuring that the time-averaged values do not change by increasing the number of cycles used in the averaging.

For all A_R, Fig. 11 shows that the amplitude of C_T as well as C_L increases with an increase in λ^*. This could be attributed to the lift-based accelerating/decelerating type of thrust generation for the pitching as compared to a continuous thrust generation for the undulating motio; similar variation was obtained for a 2D undulating/pitching hydrofoil considered in our recent study [2]. Further, the jet flow within the vortex rings for the smaller λ^* based undulation is weaker and more inclined toward the horizontal as compared to the almost vertical stronger jet flow within the vortex rings and horseshoe vortex for the larger λ^* based pitching. This leads to the larger amplitudes of C_T and C_L for the larger λ^*. Note from Fig. 11 that the amplitude of C_T is almost the same for the $\lambda^* = 4.0$ and ∞, whereas there is a considerable difference in the amplitude of C_L. Furthermore, the mean value of C_T decreases with increasing λ^* from 4.0 to ∞. This is due to the complicated vortex structure reported for the larger λ^*, which leads to a reverse flow.

With increasing A_R, Fig. 11 shows that the amplitude of C_T as well C_L increases. For C_T, note that the increase in the maximum value of C_T is larger as compared to the decrease in the minimum value of C_T; a similar observation was made by Dong *et al.* [24], for pitching and heaving ellipsoids.
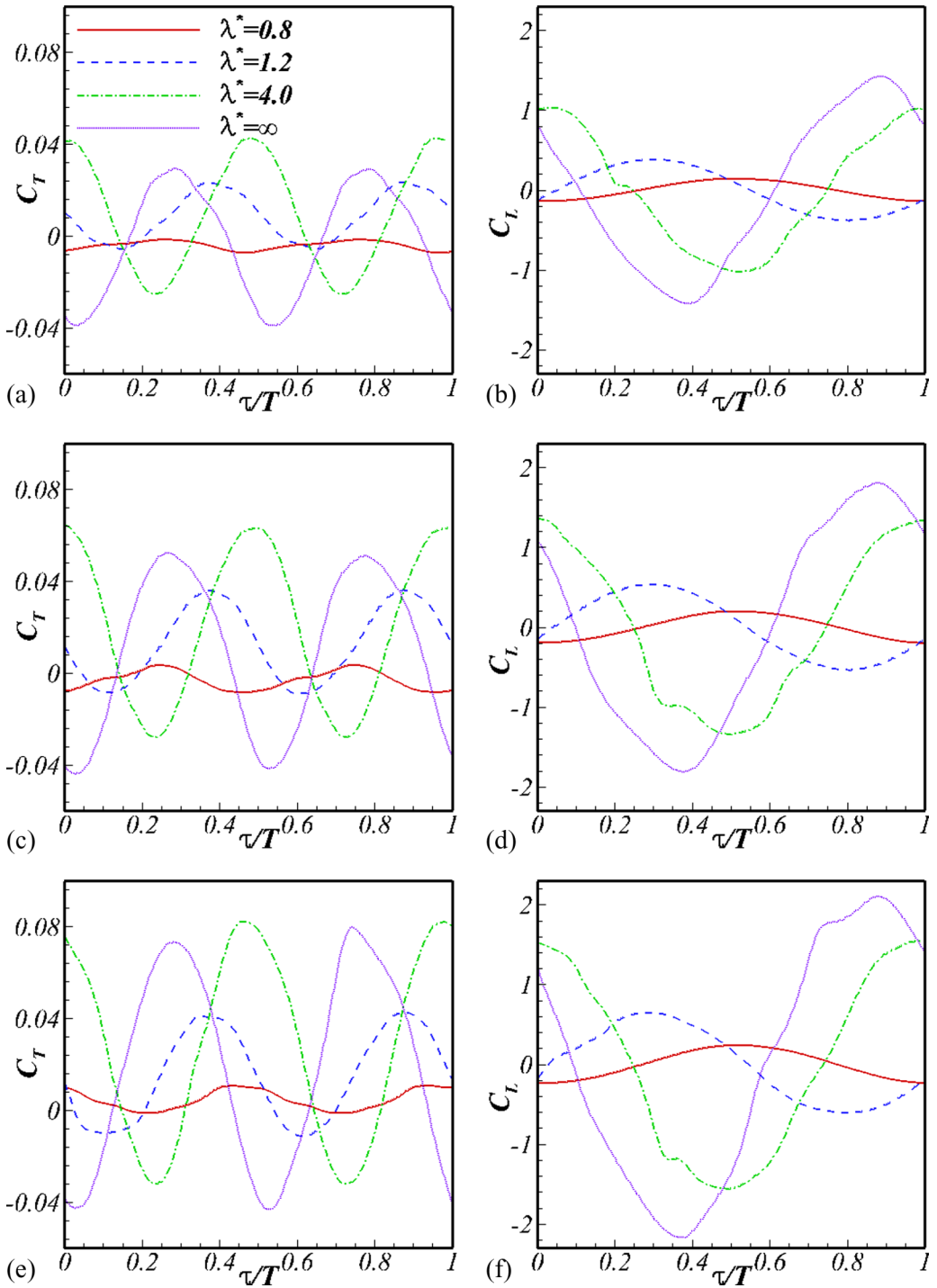
FIG. 11. Temporal variation of instantaneous (a),(c),(e) thrust coefficient C_T and (b),(d),(f) lift coefficient C_L, with increasing λ^* during one cycle of undulation/pitching, at (a),(b) $A_R = 0.5$, (c),(d) $A_R = 0.75$, and (e),(f) $A_R = 1.0$ for Re $= 10\,000$, St $= 0.5$, and $A_{\max} = 0.15$.
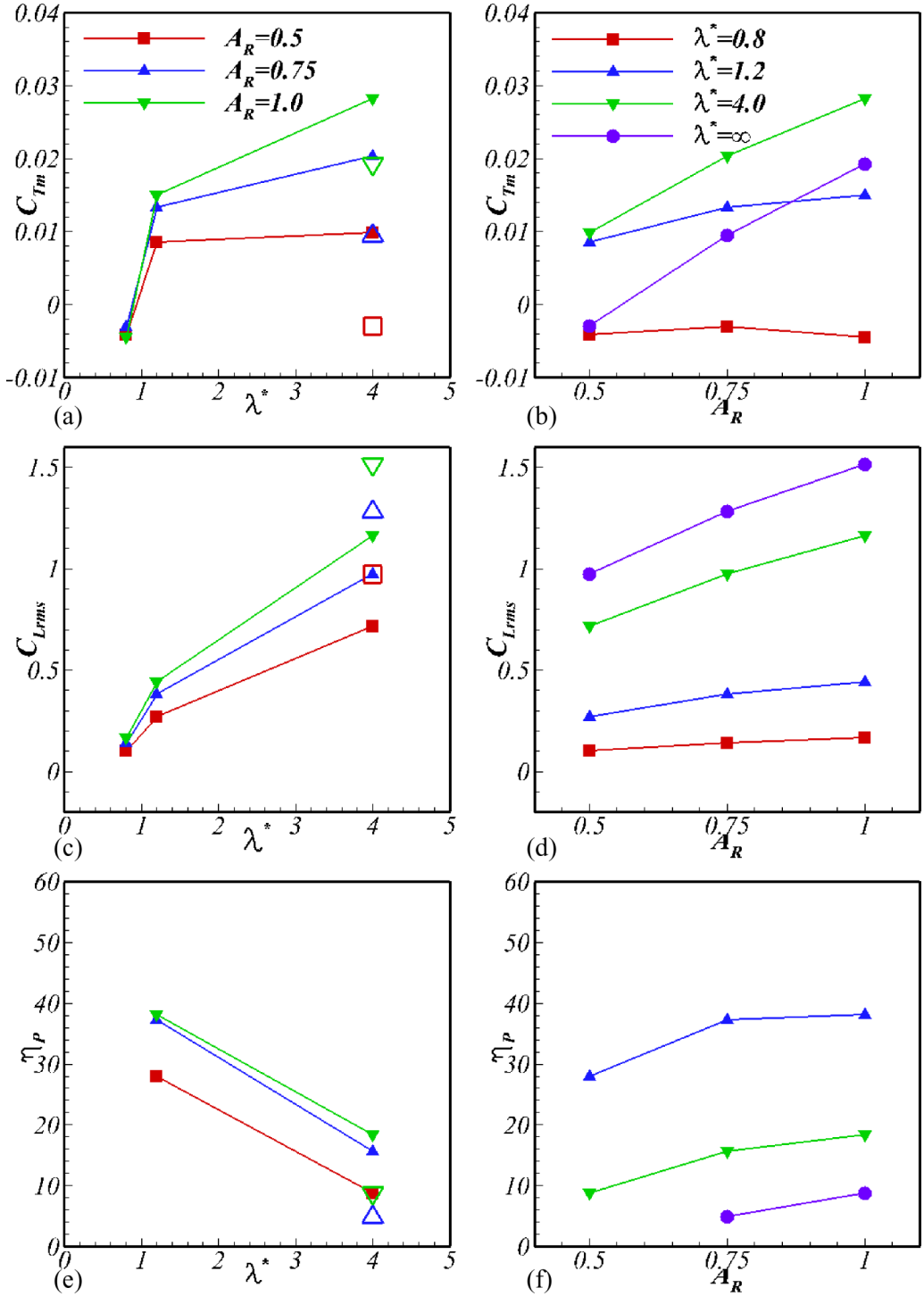
FIG. 12. Variation of the (a),(b) mean thrust coefficient C_{Tm}, (c),(d) rms value of lift force coefficient C_{Lrms}, and (e),(f) propulsive efficiency η_P with increasing (a),(c),(e) λ^* and (b),(d),(f) A_R, for the batoid fishlike locomotion at St = 0.5, $A_{max} = 0.15$, and Re = 10 000. Unfilled symbols in (a), (c), and (e) represent the values corresponding to the pitching motion of the hydrofoil cross section ($\lambda^* \to \infty$).

This results in the net increase in the time-averaged value C_{Tm} with increasing A_R. This could be attributed to larger vortex rings and horseshoe vortex at the larger A_R.

At various values of A_R, Fig. 12 shows that the mean thrust coefficient C_{Tm} and rms value of lift force coefficient C_{Lrms} increases while the propulsive efficiency η_p decreases monotonically with λ^* increasing from 0.8 to 4.0. The figure also shows the unfilled symbols for the values of all the parameters at $\lambda^* = \infty$. At various A_R, it is interesting to note from Fig. 12(a) that the mean thrust coefficient C_{Tm} for $\lambda^* = \infty$ as compared to $\lambda^* = 4.0$ is smaller. This *indicates* that there is an optimum value of λ^* at which C_{Tm} is maximum for the batoid fishlike locomotion as compared to a monotonic asymptotic increase in C_{Tm} (with increasing λ^*) for BCF types of fish, in our recent study [2]. The optimum λ^* can be attributed to the relative strength of vortex rings and horseshoe vortex. For smaller λ^*, only vortex rings are present, and the jet flow within the rings, as shown in Fig. 8, results in thrust generation. With increasing λ^*, the figure shows that the horseshoe vortex formation results in additional thrust generation leading to an increase in C_{Tm}. With a further increase in λ^*, the ring formation is disturbed by the interaction of streamwise vortices from different cycles (explained later in Sec. VII B) resulting in multiple ring formation; the complex vortex structure leads to a reduction in C_{Tm}. At the optimum λ^*, the combination of horseshoe vortex and vortex rings are such that it leads to the maximum C_{Tm}. However, with increasing λ^* from 0.8 to ∞, the monotonic increase in Fig. 12(c) indicates that C_{Lrms} is almost unaffected by the multiple ring formation since the vertical force due to the horseshoe vortex is very large as compared to the vortex rings. Figure 12(e) does not show the propulsive efficiency η_P at $\lambda^* = 0.8$ due to a drag generation, and the maximum value of η_P is seen at an intermediate wavelength $\lambda^* = 1.2$. This is because of the smooth vortex ring and combined thrust generation by the horseshoe vortex and vortex ring [Figs. 8(d)–8(f)]. Thus, it can be concluded that moderate chordwise flexibility of the hydrofoil cross section is required for optimal propulsive performance (maximum thrust force and efficiency) of batoidlike locomotion.

With increasing A_R, Fig. 12 shows that C_{Tm}, C_{Lrms}, and η_p increases for all λ^* except at the smallest $\lambda^* = 0.8$ for C_{Tm} that decreases slightly after $A_R = 0.75$. The multiple vortex ring formation at larger A_R [Fig. 8(c)] results in almost vertical jet formation leading to an increase in C_{Lrms} with increasing A_R. Figures 12(b) and 12(d) show that the increase in C_{Tm} and C_{Lrms} with increasing A_R is much larger at larger λ^*. This is because, at larger λ^*, C_{Tm} and C_{Lrms} are mainly dependent on the stronger horseshoe vortex (as compared to the weaker vortex rings) which becomes stronger with increasing A_R.

VI. EFFECT OF FREQUENCY OF THE PERIODIC 3D KINEMATICS FOR *DASYATIS* AND A HYPOTHETICAL BATOID FISH

A. Instantaneous flow pattern

With increasing nondimensional frequency St for both the $\lambda^* = 0.8$ and ∞, Fig. 13 shows a transition in the vortex structure from a single row of vortices (at St $= 0.2$) to a double row of vortices (at St $= 0.5$ and 0.7). The vortex rings in each half-cycle are connected directly at the smallest St $= 0.2$ [Figs. 13(a) and 13(b)]. In contrast, a vortex contrail is present at the largest St [Figs. 13(c)–13(f)]. This is because of the smaller vertical-induced velocity of vortex rings due to a weaker vertical jet at the smaller St. The vortex ring does not move in the vertical direction. The direction of induced velocity in Figs. 13(a) and 13(b) indicates that the vortex structure is of drag producing type; the arrow shown in Fig. 13(a) is the slightly upstream inclined jet flow within the vortex. Further, the smaller St results in longer and stretched vortex rings that indicate a weaker jet flow within the vortex rings as compared to a stronger jet flow at larger St. With increasing St, the strength of the vortex ring increases and spacing between the vortices decreases. At the larger St, the smaller spacing between the vortex rings results in the connection of vortex rings from the previous cycle [Fig. 13(e)]. Further, with increasing St, an increase in the strength of the trailing edge spanwise vortex results in the formation of a horseshoe type of vortex even at smaller
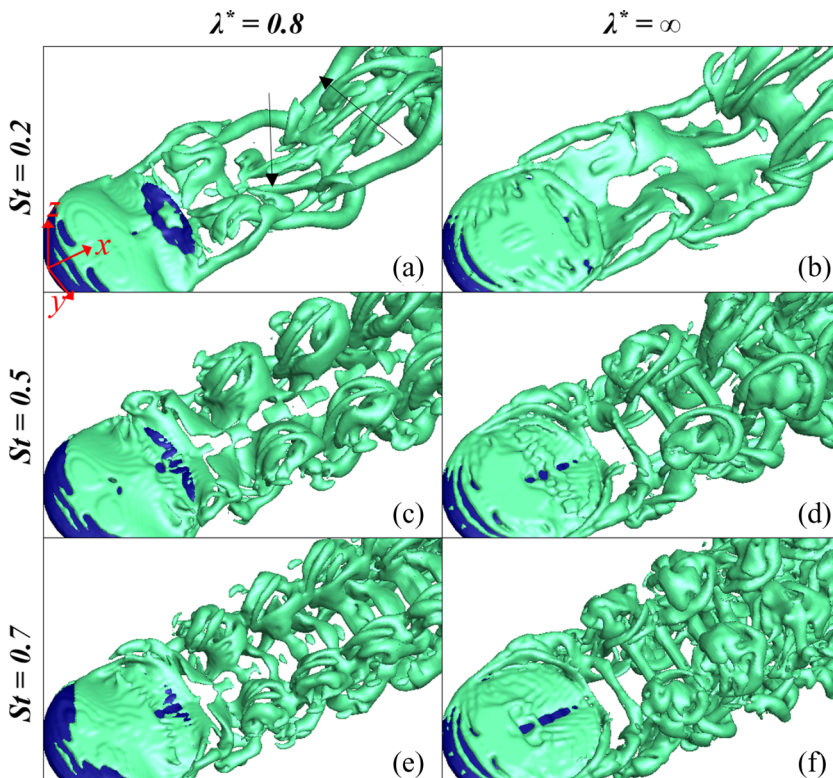
FIG. 13. Effect of nondimensional frequency of undulation/pitching St on the instantaneous Q-criterion based 3D vortex structure of the batoid fishlike locomotion for $\lambda^* = 0.8$ and $\lambda^* = \infty$, at $A_R = 1.0$, $A_{\max} = 0.15$, and Re = 10 000.

λ^* [Fig. 13(e)] that leads to an enhancement in the hydrodynamic forces. Also, at larger St, the combination of vortex rings from different cycles increases the lift force.

After the 3D vortex structure for various St at $\lambda^* = 0.8$ and ∞, the 2D contours (at $Y = 0.25A_R$) are shown in Figs. 14 and 15 for the spanwise vorticity and streamwise velocity, respectively. As discussed above for Fig. 13, where a single- (double-) row vortex structure is observed at smaller (larger) λ^*, the corresponding 2D vorticity contours are shown in Fig. 14. The vortex rings from both half-cycles join together without a vortex contrail [shown marked in Fig. 14(a)] for the smaller St leading to a single-row vortex. The corresponding U-velocity contour in Figs. 15(a) and 15(b) shows a drag producing straight wake at the smallest St as compared to thrust producing two jets on both sides in Figs. 15(c)–15(f), for the double-row vortex structure at the largest St. Further, at the larger St, the vortices come closer together, and multiple vortex rings start appearing [Fig. 14(e)]. Further, the horseshoe vortex also starts appearing at the larger St. This increases the strength of the jet flow [Fig. 15(e)]. For larger λ^*, the horseshoe vortex structure and multiple vortex ring formations start even at an earlier St [Fig. 14(d)].

B. Propulsive performance parameters

With increasing St, Fig. 16 shows a monotonic increase in the mean thrust coefficient C_{Tm} and rms value of the lift force coefficient C_{Lrms}, with a larger value of C_{Tm} and C_{Lrms} at $\lambda^* = \infty$ as compared to $\lambda^* = 0.8$. This increase in the propulsive performance parameters could be attributed to the increase in strength of the jet flow with increasing St and λ^*. Note that the variation of C_{Tm}
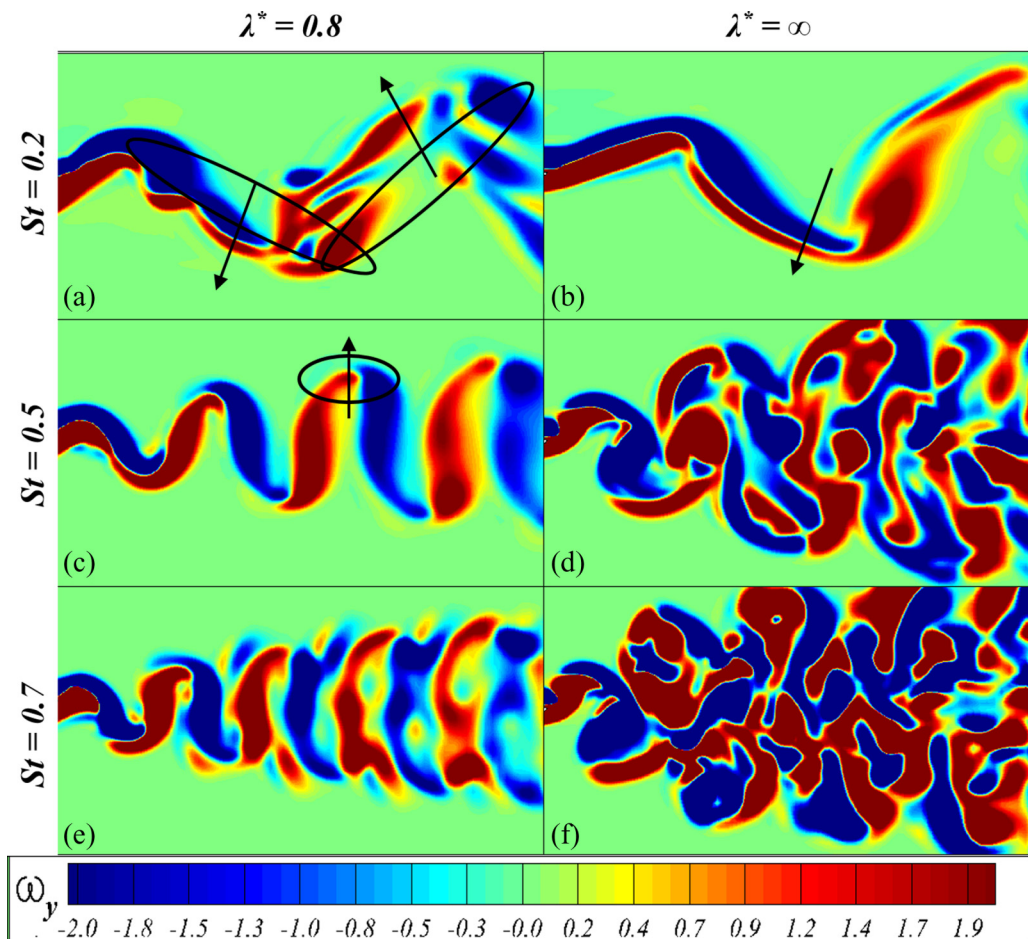
FIG. 14. Effect of nondimensional frequency of undulation/pitching St on the instantaneous spanwise vorticity (ω_y) contours (at $Y = 0.25A_R$) of the batoid fishlike locomotion for $\lambda^* = 0.8$ and $\lambda^* = \infty$, at $A_R = 1.0$, $A_{\max} = 0.15$, and Re = 10 000.

with St is found almost linear for the $\lambda^* = 0.8$ and quadratic for $\lambda^* = \infty$. This is because the thrust generation in undulation is by pushing the fluid by the wave motion; whereas for $\lambda^* = \infty$, the thrust generation is by the accelerating/decelerating pendulumlike motion [2]. Thus, similar to the results reported in our recent 2D study [2] on fishlike undulating hydrofoil, C_{Tm} scales with the wave velocity ($\sim \lambda^* \mathrm{St}$) for the undulation at $\lambda^* = 0.8$, and the acceleration of the body ($\sim \mathrm{St}^2$) for the pitching at $\lambda^* = \infty$.

VII. PERIODIC 3D VORTICITY DYNAMICS FOR THE BATOID FISHLIKE LOCOMOTION

This section presents the temporal variation of the Q-criterion based 3D vortex structure, within one time period of the batoid fishlike 3D kinematics, at St = 0.5 and $A_{\max} = 0.15$. Furthermore, the results are for the batoid fishlike body with aspect ratio $A_R = 1.0$ (of the ellipse-shaped top cross section) and the tethered propulsion at Re = 10 000. The periodic 3D vorticity dynamics are presented in separate sections below, for the largest chordwise flexibility and the smallest flexibility based $\lambda^* = \infty$, simulated here for a real and a hypothetical batoid fish, respectively.
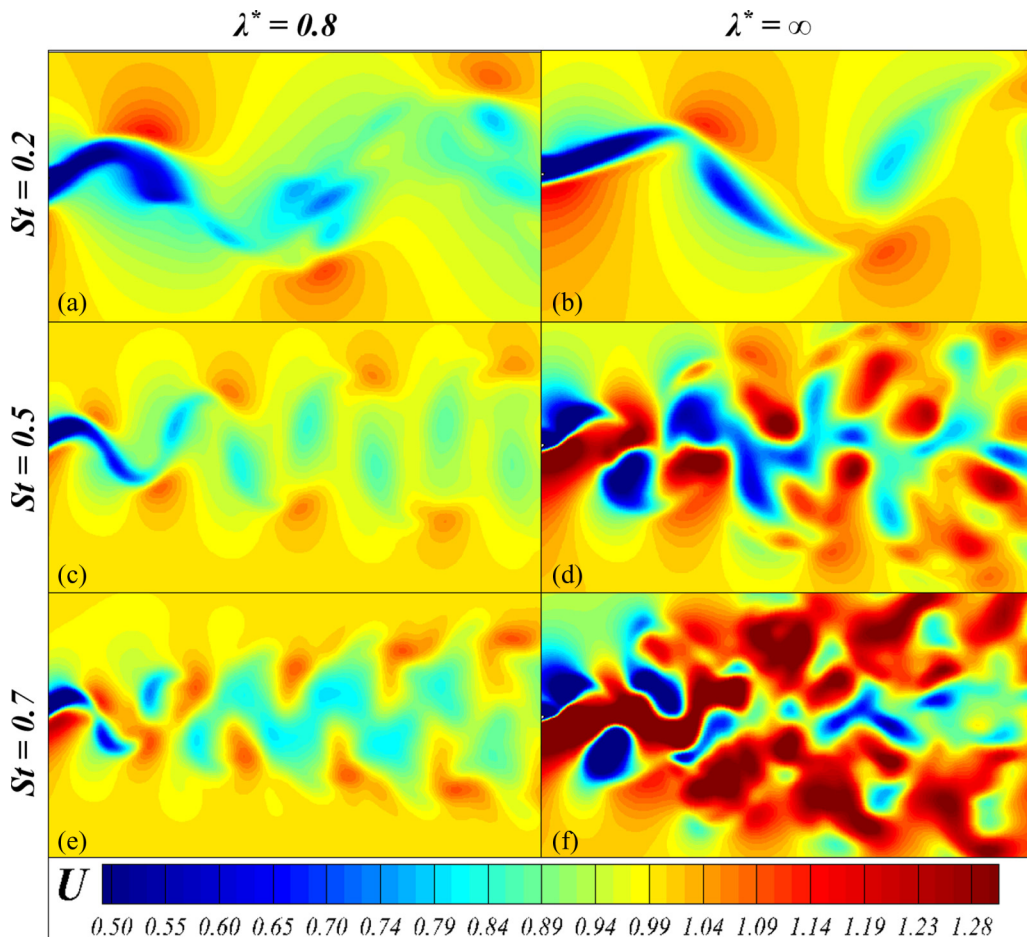
FIG. 15. Effect of nondimensional frequency of undulation/pitching St on the instantaneous streamwise velocity (U) contours (at $Y = 0.25A_R$) of the batoid fishlike locomotion for $\lambda^* = 0.8$ and $\lambda^* = \infty$, at $A_R = 1.0$, $A_{\max} = 0.15$, and Re $= 10\,000$.

A. Largest chordwise flexibility based *Dasyatis* type of batoid fish

For the smallest wavelength $\lambda^* = 0.8$ and the largest chordwise flexibility based undulating motion of the hydrofoil-shaped cross section of the *Dasyatis sabina* fishlike tethered propulsion, Fig. 17 shows that the 3D vortex structure consists of the vortex rings connected by contrails. The 3D vortex structure is symmetric about the plane of symmetry ($y = 0$), due to a spanwise symmetric kinematics of both the motion—the undulating motion in the frontal x-z plan—and the two-sided pitching motion in the streamwise y-z plane. The spanwise symmetric undulating motion (in the frontal and back planes) results in the formation of *trailing edge spanwise vortex (TESPV)* ω_y, marked as red arrows in Fig. 17(a). Whereas, the spanwise two-sided symmetric-pitching motion results in the formation of *side streamwise vortex (SSTV)* ω_x, on the front and back sides of the body, that is marked as blue arrows on the two sides in Fig. 17(a). Similar TESPV and SSTV were presented by Dong *et al.* [24], for the pitching and heaving ellipsoid.

In addition to these two vortices, the two-sided symmetric-pitching motion here results in streamwise vortices ω_x near the plane of symmetry, called here as *midplane streamwise vortices (MPSTV)* that are marked as yellow arrows in Fig. 17(a). The SSTV and MPSTV on the front side as compared to those on the backside of the batoid fishlike body are of opposite sign, as shown in
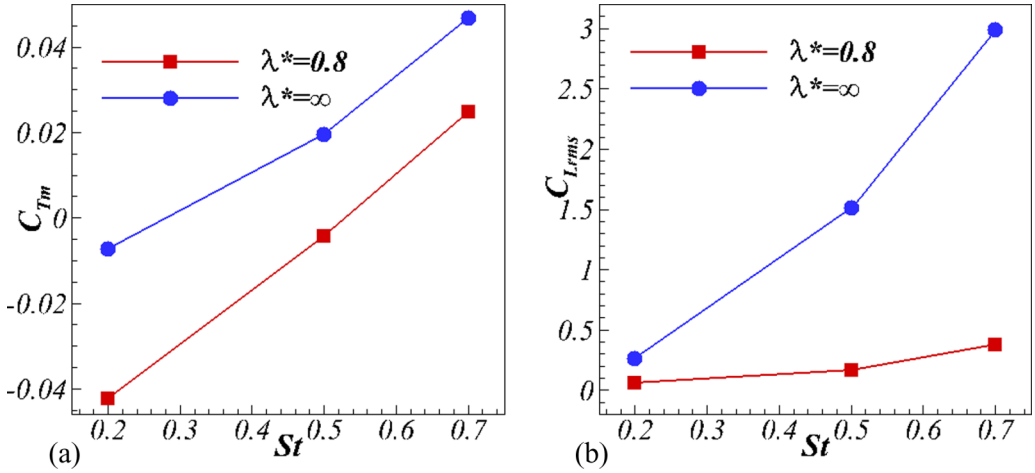
FIG. 16. Variation of the (a) mean thrust coefficient C_{Tm} and (b) rms value of lift force coefficient C_{Lrms} with increasing St for $\lambda^* = 0.8$ and $\lambda^* = \infty$, at $A_R = 1.0$, Re $= 10\,000$, and $A_{max} = 0.15$.

Fig. 17(a). These streamwise vortices are about to shed when the tip of the tail reaches the maximum vertical displacement [Fig. 17(b)]. When the vortices move further downstream, the spanwise vortex TESPV ω_y (red arrows) together with the streamwise vortices from the sides SSTV ω_x (blue arrow) and the plane of symmetry MPSTV ω_x (yellow arrow) forms vortex rings on both sides of the plane of symmetry, as shown marked in Fig. 17(c). Thus, one vortex ring is formed on each of the two sides of the body in a half-cycle of the undulation (corresponding to the motion of the trailing edge of the foil from the mean to the topmost and back to the mean position). Similarly, two vortex rings are formed on the bottom side during the next half-cycle [Fig. 17(d)]. When the streamwise vortices combine to form the vortex ring near the trailing edge, a spanwise vortex of opposite sign (clockwise) starts forming at the same place [Fig. 17(d)]. This results in the stretched vortices leading to the formation of a vortex contrail between the two rings [Fig. 17(d)], as discussed above, with the help of the schematics in Fig. 7.

A zoomed view of the 3D vortex structure in Fig. 17(b) is shown in Figs. 17(e)–17(g), demonstrating the various vortices and vortex rings, on one of the sides (midplane to front side) of the body, more clearly. The figure shows that the TESPV, together with the side SSTV and MPSTV (represented by red, blue, and yellow arrows in Figs. 17(e)–17(g)], forms the vortex ring. A jet flow [represented by dotted black arrows in Fig. 17(f)], within the rings, leads to the thrust generation. Further, the vortex rings in Fig. 17 are not as smooth; this may be due to a larger Reynolds number and a phase difference between the undulating and the pitching motions that also results in a more deformed shape of vortex ring as compared to the smooth vortex ring reported by Dong *et al.* [24].

B. Smallest chordwise flexibility based hypothetical batoid fish

For the largest wavelength $\lambda^* = \infty$ and the smallest flexibility based pitching motion of the hydrofoil-shaped cross section of the hypothetical batoid fishlike tethered propulsion, Fig. 18 shows that the 3D vortex structure is substantially different from that at the smallest wavelength $\lambda^* = 0.8$ based undulating motion (Fig. 17). Figure 18(b) shows that the SSTV on the front and back sides together with TESPV forms a horseshoe vortex that was not found for the smallest wavelength.

The horseshoe vortex formation is similar to the finite span pitching foils [5]. This can be attributed to a stronger TESPV formation at the larger wavelength as compared to the smaller wavelength. For the smaller wavelength, since both spanwise vortices and streamwise vortices are of almost the same magnitude, both the vortices combine and form vortex rings. Whereas, for larger
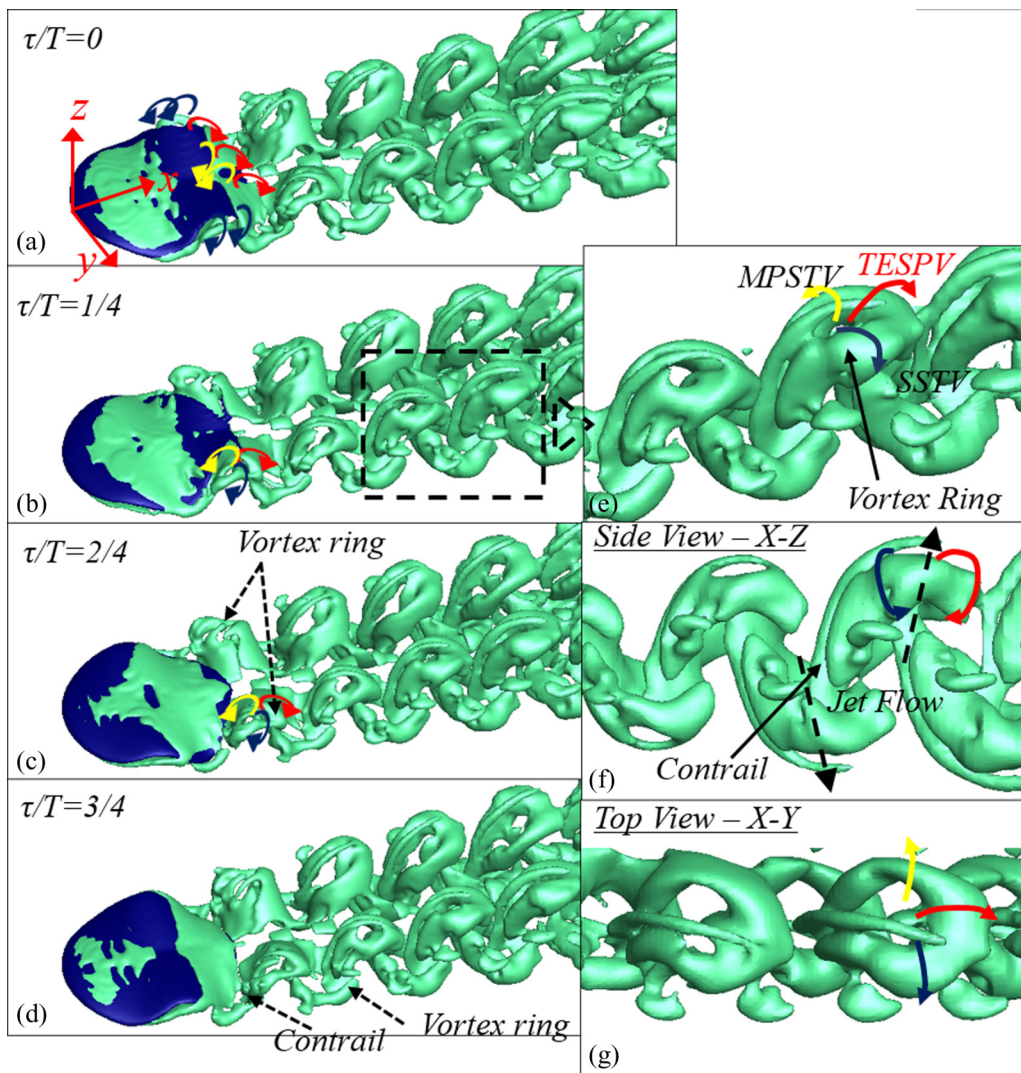
FIG. 17. (a)–(d) Temporal variation of Q-criterion based 3D vortex structure within one time period of the periodic 3D kinematics for the batoid fishlike locomotion at $\lambda^* = 0.8$, $A_R = 1.0$, St = 0.5, $A_{max} = 0.15$, and Re = 10 000. Zoomed views of (b) are shown in (e)–(g): (e) 3D, (f) side, and (g) top views. Note that the zoomed view shows the spanwise symmetric 3D vortex structure in one of the sides, from the midplane to the front side. Here, the red arrow represents the trailing edge spanwise vortex (TESPV) ω_y, the blue arrow represents side streamwise vortex (SSTV) ω_x, and the yellow arrow represents the y midplane streamwise vortex (MPSTV) ω_x. The time instant corresponding to each subfigure is marked in the top left corner.

λ^*, a comparatively larger strength of TESPV together with SSTV forms the horseshoe type vortex. Furthermore, the strength of MPSTV is found to be almost negligible in this case; and thus, the relative strength of streamwise and spanwise vortices decides the vortex structure. With increasing λ^*, the relative strength of the spanwise vortex increases. In addition to the horseshoe vortex, the vortex rings are also formed on the front and back sides of the body. The spanwise and streamwise vortices split into two parts; the major part forms the horseshoe vortex and the rest forms vortex rings, as shown in Fig. 18(a). Unlike the smallest $\lambda^* = 0.8$, multiple streamwise and spanwise vortices result in multiple vortex rings at the largest $\lambda^* = \infty$.
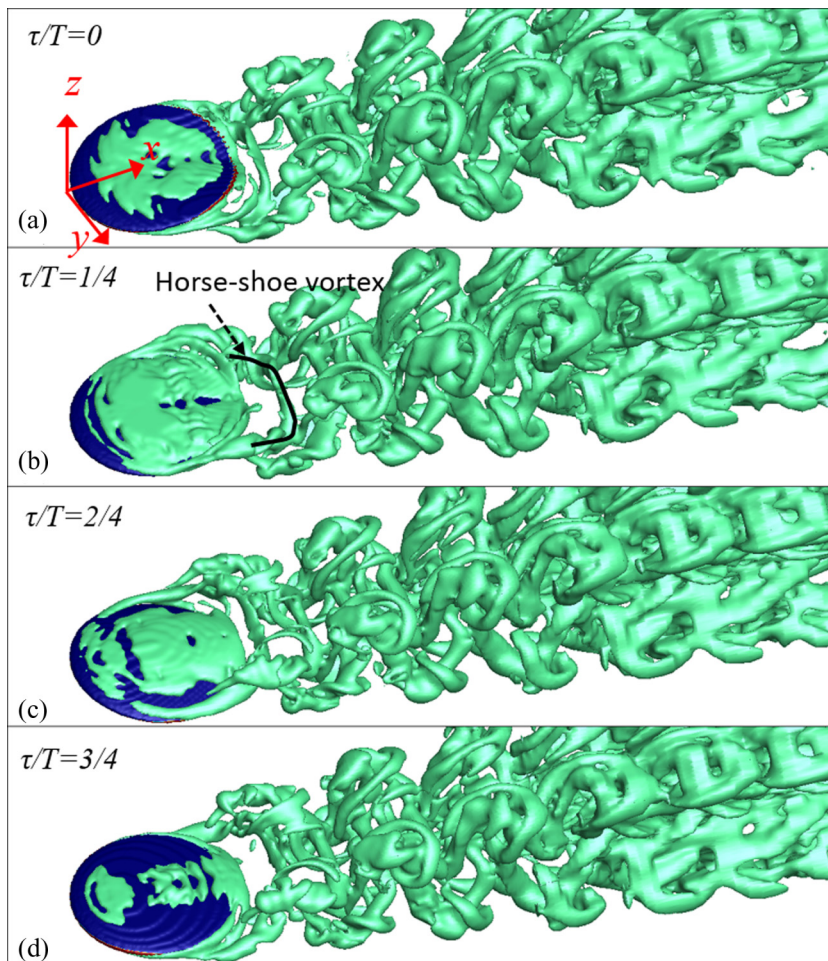
FIG. 18. Temporal variation of Q-criterion based 3D vortex structure within one time period of the periodic 3D kinematics for the batoid fishlike locomotion at $\lambda^* = \infty$, $A_R = 1.0$, St $= 0.5$, $A_{max} = 0.15$, and Re $= 10\,000$. The time instant corresponding to each subfigure is marked in the top left corner.

Figure 18(a) shows the time instant at which the horseshoe vortex is just shed. When the vortex moves downward, the spanwise vortex and streamwise vortex split into two parts [Figs. 18(b) and 18(c)]. The split parts of the vortices form rings over the horseshoe vortex [Fig. 18(d)]. Further, the streamwise vortices formed are in the directed upward and downward directions by the wavy motion for the smaller λ^* based undulation. When the vortex ring is formed, the streamwise vortex is directed upward in the first half of the cycle, and it is directed downward in the next half-cycle of pitching, leading to comparatively smooth vortex rings. For larger λ^*, the streamwise vortex formed, during both halves of the cycle, combines and forms a complicated vortex structure. This probably results in poor propulsive efficiency of the larger wavelength (Fig. 12).

VIII. SUMMARY OF THE HYDRODYNAMICS STUDY

The summary of our 3D vortex structures and the induced jet flow are presented here with the help of a schematic in Fig. 19. For a smaller λ^*, Fig. 19(a) shows that the streamwise undulating motion results in spanwise vortices on the trailing edge (TESPV), and the two-sided symmetric-pitching
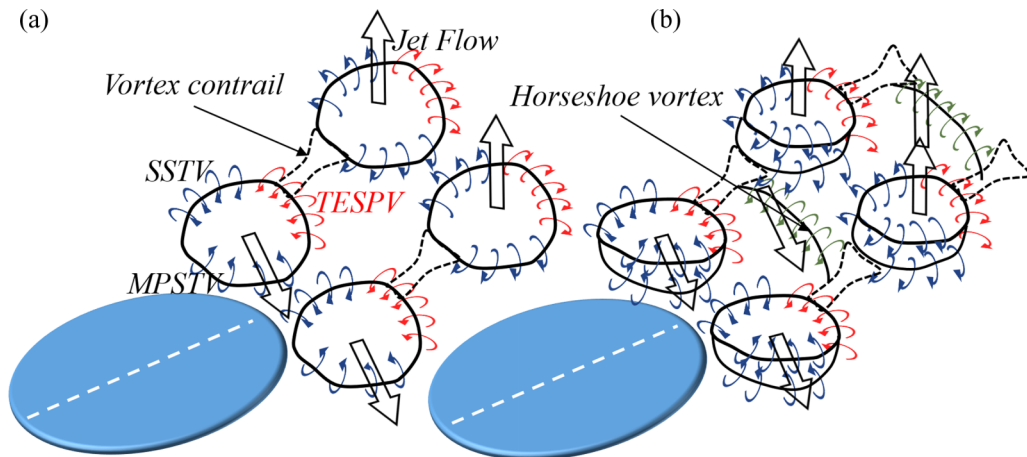
FIG. 19. Schematic representation of the spanwise symmetric 3D vortex structures and the induced jet flow, obtained in the present work, at (a) smaller λ^* and (b) intermediate as well as larger λ^*. The various vortices marked as TESPV, SSTV, and MPSTV correspond to trailing edge spanwise vortex, side streamwise vortex, and midplane streamwise vortex, respectively. The block arrows represent the direction of a jet flow induced by a vortex ring (formed by the combination of TESPV, SSTV, and MPSTV) and the horseshoe vortices.

motion results in streamwise vortices on the sides and the plane of symmetry (SSTV and MPSTV). The TESPV, SSTV, and MPSTV together form a vortex ring in each half-cycle of the 3D kinematics. Note that the MPSTV is absent in a 2D kinematics, involving pitching and heaving (both the motions on a single plane) ellipsoids, proposed in the literature [24]. Thus, a single vortex ring connecting the SSTV on both the sides are reported for the 2D kinematics [24] as compared to the symmetric vortex rings found here for the 3D kinematics.

For the intermediate λ^*, Fig. 19(b) shows that the vortex rings formed are complex as compared to the smaller λ^*, and there is an additional horseshoe vortex connecting the vortex contrails from both sides of the spanwise midplane. For the larger λ^*, the flow structure is similar to that shown in Fig. 19(b); however, the vortex rings are more complex, and the strength of the horseshoe vortex is larger. This is because the streamwise wavy motion at smaller λ^* helps in directing the vortices to the upper and lower sides, leading to smoother vortex rings; whereas, for the larger wavelength, absence of the proper direction leads to the complicated vortex structure.

For various λ^*, Fig. 19 shows a downstream inclined almost upward (downward) jet flow within the vortex rings formed on the upper (lower) sides, leading to the thrust generation. For the intermediate λ^*, a jet flow is also induced due to the horseshoe vortex structure [Fig. 19(b)], leading to enhancement in the thrust force. However, the vortex-rings-induced jet flow strength reduces at larger λ^*, due to complex vortex structures in the vortex rings. Thus, the maximum thrust force is obtained for the optimum combination of the jet flow induced by the vortex rings and the horseshoe vortex. For the larger λ^*, the more complex vortex rings result in a reduction in the resultant thrust force.

IX. CONCLUSIONS

Various types of batoid fishlike locomotion are modeled by a 3D unified-kinematics model for a spanwise symmetric 3D kinematics—two-sided pitching and undulating motions in orthogonal cross sections. The two-sided (front and back) pitching motion is a batlike flapping of the various streamwise cross sections, and the undulation is a muscles-induced chordwise flexibility based stream-wise traveling wave motion along the various hydrofoil-shaped lateral cross sections. By

varying the nondimensional wavelength λ^* of the wavy undulation from 0.8 to ∞, various types of real and hypothetical batoid fish are realized. The effect of the muscles-induced chordwise flexibility λ^* of the wavy undulation of the hydrofoil-shaped frontal cross section, aspect ratio A_R of the spanwise ellipse, and nondimensional frequency of the 3D kinematics St, on the hydrodynamic characteristics and propulsive performance of various types of batoid fish, are studied at a constant Reynolds number Re = 10 000 and nondimensional maximum amplitude $A_{max} = 0.15$.

The following conclusions are drawn from this three-dimensional biological hydrodynamics study:

(1) For smaller λ^* based *Dasyatis* type of batoid fish, a double-row vortex structure with almost smooth vortex rings on both sides of the midplane is obtained; whereas, for intermediate λ^* based *Rhinoptera bonasus* type of batoid fish, a horseshoe vortex (connecting streamwise vortices from the edges) is also obtained along with multiple ring formation on both sides of the midplane. The combined horseshoe vortex and vortex ring is not found in the literature, and is presented here as a new flow structure for the present class of problem. Jet flows obtained within the rings and horseshoe vortex result in the thrust generation.

(2) In contrast to the BCF types of fish, for the batoid fish, the maximum thrust coefficient is found at an intermediate wavelength λ^*. The larger thrust force is due to the presence of smoother vortex rings and horseshoe vortex, and the force reduces due to the formation of multiple vortex rings at larger λ^*. The rms value of lift force C_{Lrms} is found increasing monotonically with λ^*. This is due to the dominating effect of a vertical jet (induced by the horseshoe vortex) over the multiple rings. Since the jet is almost vertical for the larger λ^*, the magnitude of lateral force is very large as compared to the thrust force. Thus, reduction in the hydrodynamic force due to multiple vortex ring formation does not affect the lift force while it results in a reduction in the thrust force.

(3) With increasing aspect ratio A_R, the thrust force increases monotonically for various λ^* (except at $\lambda^* = 0.8$ where it is almost constant). This is because the strength of the horseshoe vortex is larger at larger A_R and λ^*.

(4) For the 3D kinematics of the *Dasyatis* and a hypothetical batoid fish, the 3D vortex structure changes from a single-row to a double-row type of structure. The results are significant as it presents various types of flow structures and relates them to the propulsive performance parameters for efficient swimming of various types of batoid fish, which could be used for the design of underwater vehicles.

---

[1] M. Sfakiotakis, D. M. Lane, and J. B. C. Davies, Review of fish swimming modes for aquatic locomotion, IEEE J. Oceanic Eng. **24**, 237 (1999).

[2] N. Thekkethil, A. Sharma, and A. Agrawal, Unified hydrodynamics study for various types of fishes-like undulating rigid hydrofoil in a free stream flow, Phys. Fluids **30**, 077107 (2018).

[3] L. J. Rosenberger and M. W. Westneat, Functional morphology of undulatory pectoral fin locomotion in the stingray *Taeniura lymma* (chondrichthyes: Dasyatidae), J. Exp. Biol. **202**, 3523 (1999).

[4] L. J. Rosenberger, Pectoral fin locomotion in batoid fishes: Undulation versus oscillation, J. Exp. Biol. **204**, 379 (2001).

[5] K. D. von Ellenrieder, K. Parker, and J. Soria, Flow structures behind a heaving and pitching finite-span wing, J. Fluid Mech. **490**, 129 (2003).

[6] J. H. J. Buchholz and A. J. Smits, On the evolution of the wake structure produced by a low-aspect-ratio pitching panel, J. Fluid Mech. **546**, 433 (2006).

[7] J. H. J. Buchholz and A. J. Smits, The wake structure and thrust performance of a rigid low-aspect-ratio pitching panel, J. Fluid Mech. **603**, 331 (2008).

[8] M. A. Green, C. W. Rowley, and A. J. Smits, The unsteady three-dimensional wake produced by a trapezoidal pitching panel, J. Fluid Mech. **685**, 117 (2011).

[9] J. T. King, R. Kumar, and M. A. Green, Experimental observations of the three-dimensional wake structures and dynamics generated by a rigid, bioinspired pitching panel, Phys. Rev. Fluids **3**, 034701 (2018).

[10] S. Bi and Y. Cai, Effect of spanwise flexibility on propulsion performance of a flapping hydrofoil at low Reynolds number, Chin. J. Mech. Eng. **25**, 12 (2012).

[11] C. Li and H. Dong, Three-dimensional wake topology and propulsive performance of low-aspect-ratio pitching-rolling plates, Phys. Fluids **28**, 071901 (2016).

[12] A. Hemmati, T. Van Buren, and A. J. Smits, Effects of trailing edge shape on vortex formation by pitching panels of small aspect ratio, Phys. Rev. Fluids **4**, 033101 (2019).

[13] R. P. Clark and A. J. Smits, Thrust production and wake structure of a batoid-inspired oscillating fin, J. Fluid Mech. **562**, 415 (2006).

[14] K. W. Moored, W. Smith, J. M. Hester, W. Chang, and H. Bart-Smith, Investigating the thrust production of a myliobatoid-inspired oscillating wing, *Advances in Science and Technology* (Trans Tech Publications, 2008), Vol. 58, pp. 25–30.

[15] W.-s. Chen, Z.-j. Wu, J.-k. Liu, S.-j. Shi, and Y. Zhou, Numerical simulation of batoid locomotion, J. Hydrodyn. **23**, 594 (2011).

[16] P. A. Dewey, A. Carriou, and A. J. Smits, On the relationship between efficiency and wake structure of a batoid-inspired oscillating fin, J. Fluid Mech. **691**, 245 (2012).

[17] K. W. Moored, P. A. Dewey, A. J. Smits, and H. Haj-Hariri, Hydrodynamic wake resonance as an underlying principle of efficient unsteady propulsion, J. Fluid Mech. **708**, 329 (2012).

[18] G. Iosilevskii, Hydrodynamics of the undulatory swimming gait of batoid fishes, Eur. J. Mech.-B/Fluids **45**, 12 (2014).

[19] R. G. Bottom, I. Borazjani, E. L. Blevins, and G. V. Lauder, Hydrodynamics of swimming in stingrays: Numerical simulations and the role of the leading-edge vortex, J. Fluid Mech. **788**, 407 (2016).

[20] N. Thekkethil and A. Sharma, Level set function based immersed interface method and benchmark solutions for fluid flexible-structure interaction, Int. J. Numer. Methods Fluids **91**, 134 (2019).

[21] A. Sharma, *Introduction to Computational Fluid Dynamics: Development, Application and Analysis* (Wiley & Athena UK and Ane Books Pvt. Ltd., New Delhi, 2017).

[22] N. Thekkethil, Computational fluid-structure dynamics development and its application for analysis of various types of 2D/3D fishes-like kinematics, propulsion, and flexibility, PhD. thesis, Indian Institue of Technology Bombay, 2019.

[23] T. A. Johnson and V. C. Patel, Flow past a sphere up to a Reynolds number of 300, J. Fluid Mech. **378**, 19 (1999).

[24] H. Dong, R. Mittal, and F. M. Najjar, Wake topology and hydrodynamic performance of low-aspect-ratio flapping foils, J. Fluid Mech. **566**, 309 (2006).

[25] S. Kern and P. Koumoutsakos, Simulations of optimized anguilliform swimming, J. Exp. Biol. **209**, 4841 (2006).

[26] T. Namshad, M. Srivastava, A. Agrawal, and A. Sharma, Effect of wavelength of fish-like undulation of a hydrofoil in a free-stream flow, Sādhanā **42**, 585 (2017).

[27] M. Gazzola, M. Argentina, and L. Mahadevan, Scaling macroscopic aquatic locomotion, Nat. Phys. **10**, 758 (2014).

[28] X. Chang, L. Zhang, and X. He, Numerical study of the thunniform mode of fish swimming with different Reynolds number and caudal fin shape, Comput. Fluids **68**, 54 (2012).

[29] J.-Z. Wu, H.-Y. Ma, and M.-D. Zhou, *Vorticity and Vortex Dynamics* (Springer Science & Business Media, Berlin, 2007).

[30] F. Fish, C. Schreiber, K. Moored, G. Liu, H. Dong, and H. Bart-Smith, Hydrodynamic performance of aquatic flapping: Efficiency of underwater flight in the manta, Aerospace **3**, 20 (2016).